Boundaries and defects in the cubic code

Cory T. Aitchison,[1,*] Daniel Bulmash,[2] Arpit Dua,[3,4] Andrew C. Doherty,[1] and Dominic J. Williamson[1]

[1] *Centre for Engineered Quantum Systems, School of Physics, University of Sydney, Sydney, NSW 2006, Australia*
[2] *Department of Physics and Center for Theory of Quantum Matter, University of Colorado Boulder, Boulder, Colorado 80309, USA*
[3] *Department of Physics, California Institute of Technology, Pasadena, California 91125, USA*
[4] *Institute for Quantum Information and Matter, California Institute of Technology, Pasadena, California 91125, USA*

(Received 13 October 2023; accepted 12 April 2024; published 9 May 2024)

Haah's cubic code is the prototypical type-II fracton topological order. It instantiates the no stringlike operator property that underlies the favorable scaling of its code distance and logical energy barrier. Previously, the cubic code was only explored in translation-invariant systems on infinite and periodic lattices. In these settings, the code distance scales superlinearly with the linear system size, while the number of logical qubits within the degenerate ground space exhibits a complicated functional dependence that undergoes large fluctuations within a linear envelope. Here, we extend the cubic code to systems with open boundary conditions and crystal lattice defects. We characterize the condensation of topological excitations in the vicinity of these boundaries and defects, finding that their inclusion can introduce local stringlike operators and enhance the mobility of otherwise fractonic excitations. Despite this, we use these boundaries and defects to define new encodings where the number of logical qubits scales linearly without fluctuations, and the code distance scales superlinearly, with the linear system size. These include a subsystem encoding with open boundary conditions and a subspace encoding using lattice defects.

DOI: 10.1103/PhysRevB.109.205125

I. INTRODUCTION

Quantum computers are required to operate effectively in the presence of errors and noisy operations [1–4]. A primitive component of a quantum computer is the quantum hard drive: a system capable of safely storing quantum information for long periods of time. In comparison to leading approaches such as the surface code [5,6], which require *active* procedures to continually detect and correct for errors [7], such a hard drive should be *passively* self-correcting. To this end, one can envision a system where quantum information is encoded in an energetic ground state and errors that corrupt this information are suppressed by macroscopic energy barriers [8]. Unfortunately, this behavior is impossible to achieve in many cases—such as the surface code—due to no-go theorems that prohibit self-correction in $(2+1)$D systems [8–18].

Fortunately, these theorems do not apply to higher spatial dimensions. Already in $(3+1)$D there are topological codes with no *stringlike logical operators* that have significantly better energy barriers than any $(2+1)$D code [19,20]. The earliest such example is Haah's *cubic code*, which was found via a computational search [19]. The cubic code model is part of a larger classification of unconventional topological phases of matter, known as *fracton topological orders* [19–28]. In this classification, topological codes with no stringlike operators are called type-II fracton phases [27]. As a type-II fracton phase, the cubic code only supports topological excitations that are completely immobile [19]. When used as an error-correcting code, this immobility results in a code distance that scales superlinearly with the linear system size, i.e., $d \sim \mathcal{O}(L^{\alpha})$ for $\alpha > 1$, where L is the number of lattice sites along one axis. Moreover, the minimum energy required to map between degenerate ground states via local operations—also known as the energy barrier—scales as $\mathcal{O}(\log(L))$ [29]. This energy barrier enables the cubic code to be partially self-correcting: its quantum memory time increases with the system size only up to a finite threshold that decreases with temperature [29]. For comparison, the surface code in $(2+1)$D has a memory time independent of system size. This property makes the cubic code a leading candidate for creating a quantum hard drive in $(3+1)$D.

There are, however, additional features of the cubic code that are undesirable for applications to quantum error correction (QEC). The number of encoded qubits, k, varies sporadically with the system size [20] (see Fig. 3). In an actual implementation, achieving a large k, therefore, requires the system to be from a family of carefully chosen system sizes that have large jumps between them. Moreover, the model was formulated in a translation-invariant setting with periodic boundary conditions, arranging the physical qubits on a 3-torus. This topology is not feasible in a strictly local architecture.

Since the discovery of the cubic code, there has not yet been an examination into how the model's topology or geometry may be modified, and how these modifications may affect its core characteristics, such as its no-string property or fracton topological order. A significant question is whether open boundary conditions or the inclusion of lattice defects affect the error-correcting properties of the code, either by

[*] cory.aitchison@sydney.edu.au

improving or worsening them. In other codes, including such modifications has the potential to increase the number of encoded qubits or enable additional fault-tolerant quantum gates [6,30–33]. However, in our setting, open boundary conditions and defects have the potential to introduce stringlike operators and reduce the energy barrier for logical errors.

In this work, we characterize the properties of boundaries and defects in the cubic code, including their interactions with quasiparticle excitations. We investigate whether modifying the cubic code by introducing boundaries and defects can affect the scaling of the number of qubits while maintaining the superlinear code distance and favorable energy barrier of the periodic model. We approach this with a combination of analytic arguments, visualizations, and numerical computations. For the latter, we simulate lattices with up to approximately 20^3 qubits, and assume a consistent extrapolation for larger systems.

A. Summary of results

In this paper, we consider the construction of X- or Z-type open boundaries normal to a crystallographic axis. These boundaries are gapped using *plaquette* stabilizers formed from truncated bulk X and Z cube stabilizers, respectively. Both cases exhibit two topologically distinct interactions with the fractonic excitations: X-type boundaries on the negative-oriented faces of the lattice (and Z-type on the positive faces) condense single fractons. Conversely, X-type positive faces (and Z-type negative faces) cause their corresponding fractons to gain a $(2+1)$D mobility within diagonal subsystems along the surface. These boundary layers have a direct correspondence to the 6-6-6 color code [34].

Our results demonstrate that the no-string property of the closed cubic code model is not readily retained in the presence of open boundary conditions. Because of this, it is nontrivial to construct QEC codes with open boundary conditions that have the desired superlinear code distance. Table I summarizes the different configurations of open boundary conditions considered in this paper; none contain only logical operators with superlinear weight. Notably, however, the scaling of k in all nontrivial cases is now a simple function of the linear system size L that does not exhibit large fluctuations.

It is nevertheless possible to create a cubic code with open boundary conditions that has a superlinear distance. For this, we use the *tennis ball 1* configuration from Table I. In the corresponding code, logical $\bar{X}$ and $\bar{Z}$ operators stretch between two boundaries in the $\hat{x}$ and $\hat{y}$ lattice directions, respectively. There exist logical $\bar{X}$ operators supported solely near the $+\hat{z}$ face, and $\bar{Z}$ operators near the $-\hat{z}$ face, that have linear weights. However, those further in the bulk have weight superlinear in L. A subsystem code [35,36] can be used to gauge out the logical qubits with either an $\bar{X}$ or $\bar{Z}$ that can be supported near a boundary face—thus producing a code with superlinear distance.

Alternatively, with boundary conditions that are periodic in the $\hat{z}$ direction only, we are able to construct stabilizer codes with simple linear scaling of k and a superlinear code distance without resorting to subsystem codes. This result, along with other periodic boundary condition codes, is summarized in Table II.

In addition to open boundary conditions, we study the inclusion of crystal lattice defects including vacancies, edge dislocations, and screw dislocations. Similar to the open boundaries, we focus on configurations that are aligned with the crystallographic axes. While modified stabilizer terms are provided for vacancies and edge dislocations, screw dislocations do not admit additional deformed stabilizers. We explore how condensation of fractons on defects affects the fracton mobility in the vicinity of these features. We propose several encodings using defects; configurations such as a pair of edge dislocations or multiple vacancies wrapped around a periodic boundary can form stabilizer code families with superlinear distances and a simple linear scaling of k. These results are discussed in detail in Sec. VI.

To the best of our knowledge, this work constitutes the first exploration of boundaries and defects in a type-II fracton topological order. Our results demonstrate that introducing defects and boundaries into the cubic code leads to encodings with new features that could prove advantageous over encodings based on periodic boundary conditions. This includes encodings with a number of logical qubits that scales linearly with the linear system size, without fluctuations. This work is a first step towards a general theory of translation symmetry enrichment in type-II fracton topological orders.

B. Outline of paper

This paper is organized as follows: In Sec. II we present background on quantum error-correcting codes and outline the key properties of the cubic code. In Sec. III we characterize the open boundary conditions of the cubic code. In Sec. IV we discuss constructions of superlinear-distance codes. In Sec. V we characterize the inclusion of defects—vacancies, edge dislocations, and screw dislocations. In Sec. VI we discuss the use of defects to construct superlinear-distance codes. In Sec. VII we present our conclusions. The Appendixes include a discussion of further open and periodic boundary codes (Appendix A) and defect codes (Appendix B) considered in this study. A summary of all the potential boundary encodings is provided in Tables I and II.

II. BACKGROUND

We begin with a brief review of quantum error-correcting codes and self-correcting quantum memories, before discussing the cubic code in particular.

A. Review of quantum error-correcting codes

A quantum error-correcting (QEC) code is a scheme to encode one or more quantum states within a higher-dimensional Hilbert space to provide the ability to detect and correct a class of errors. Arbitrary errors are generated by the algebra of single-qubit Pauli errors, spanned by the Pauli X and Z operators

$$X := \begin{pmatrix} 0 & 1 \\ 1 & 0 \end{pmatrix}, \qquad Z := \begin{pmatrix} 1 & 0 \\ 0 & -1 \end{pmatrix}, \tag{1}$$

written in the computational basis $\{|0\rangle, |1\rangle\}$ corresponding to the two states of a physical qubit. One approach for constructing QEC codes is to employ the *stabilizer formalism*

TABLE I. Summary of the properties for codes with open boundaries on a lattice with linear system size (L_x, L_y, L_z), showing the positive faces on the left and the negative faces on the right diagram. Red and dark red (blue and light blue) indicate X (Z) stabilizers. Vertex stabilizers are implied when three edges of the same color meet. The half-length edges at the vertices of the *triangular* configuration have vertex stabilizers but no edge stabilizers. The notation column corresponds to the $(xyz;\bar{x}\bar{y}\bar{z})$ faces of the lattice, where p indicates a periodic boundary and e and m are open boundaries that interact with e and m excitations, respectively. The final column identifies the presence of at least one logical operator ($\bar{X}$ or $\bar{Z}$) with a minimum weight that scales with the indicated function of L_x, L_y, and/or L_z.

Diagram	Notation	Name	Encoded qubits (k)	Logical weight
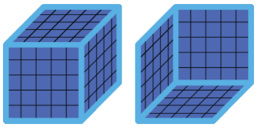	$(eee;eee)$	Only e	0	—
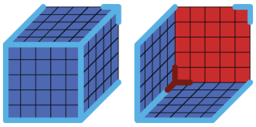	$(eee;mee)$	One (m)	0	—
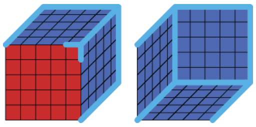	$(mee;eee)$	One (m_{ABC})	0	—
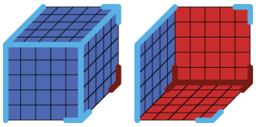	$(eee;mem)$	Two (m)	$2\min\{L_x, L_z\} - 6$	Constant, Superlinear
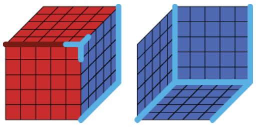	$(mem;eee)$	Two (m_{ABC})	0	—
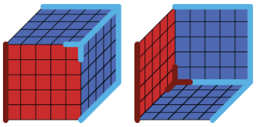	$(mee;eme)$	(m) & (m_{ABC})	0	—
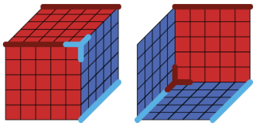	$(mem;mee)$	*Tennis ball 1*	$2L_z$	Linear, Superlinear
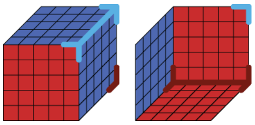	$(mee;mem)$	*Tennis ball 2*	$2L_z - 6$	Constant, Superlinear
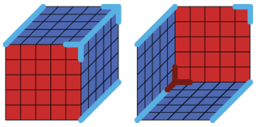	$(mee;mee)$	*Tube*	$2(L_y + L_z - L_x) - 3$	Constant, Linear, Superlinear
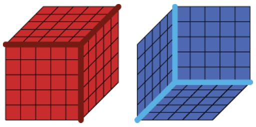	$(mmm;eee)$	*Half-half 1*	0	—
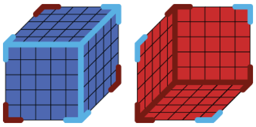	$(eee;mmm)$	*Half-half 2*	$4\min\{L_x, L_y, L_z\} - 12$	Constant, Superlinear
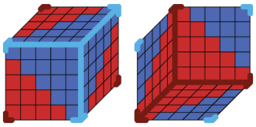	—	*Triangular*	$4L - 4,\ L = L_x = L_y = L_z$	Linear, Superlinear

TABLE II. Summary of the properties for boundary codes on a lattice with linear system size (L_x, L_y, L_z), where some direction is periodic. In cases where the behavior of anisotropic systems is unclear, we take $L_x = L_y = L_z \equiv L$. The notation column corresponds to the $(xyz; \bar{x}\bar{y}\bar{z})$ faces of the lattice, where p indicates a periodic boundary and e and m are open boundaries that interact with e and m excitations, respectively. $\tau(L_1;\ L_2)$ is a fractal-like function defined in Sec. III A 2 that encapsulates the number of stringlike operators that can form logical operators by wrapping around a periodic boundary. *Superlinearity is only ensured when $3 \nmid L_x$; otherwise, there are linear-weight operators.

Notation	Encoded Qubits (k)	Code Distance
$(ppp; ppp)$	Eq. (6)	Superlinear
$(ppe; ppe)$	$\frac{1}{2}k_{(ppp;ppp)} + 2\tau(L;\ \infty)$	Linear
$(ppm; ppe)$	$4\min\{\tau(L_x;\ L_z),\ \tau(L_y;\ L_z)\}$	Linear
$(ppe; ppm)$	0	—
$(pmm; pem)$	$2\tau(L_x;\ L_z)$	Linear
$(pem; pem)$	$2L_x$	Superlinear*
$(pem; pme)$	0	—
$(pem; pmm)$	0	—
$(pmm; pmm)$	0	—
$(pmm; pee)$	0	—
$(pee; pmm)$	0	—

[37,38]: Consider a system of n physical qubits. We select a commuting collection of (tensor) products of Pauli operators and consider the stabilizer group $\mathcal{S}$ that they generate. We require that $-I \notin \mathcal{S}$, where I is the identity operator. Quantum information is then encoded in the eigenvectors of the degenerate $+1$-eigenspace common to all elements of $\mathcal{S}$. That is, any physical measurement of the encoded state using $S_i \in \mathcal{S}$ returns a $+1$ value. Importantly, single-qubit X and Z operators anticommute with some S_i, thus mapping any encoded state out of the $+1$-eigenspace and producing a change in the measurement outcomes. This can be detected and corrected with appropriate QEC codes.

For a system with s independent stabilizer generators and n physical qubits, the degeneracy of the $+1$-eigenspace is 2^{n-s}. Equivalently, the number of encoded *logical qubits* that are protected from errors is $k = n - s$.

An effective QEC code should have a large number of encoded qubits but also should make it difficult for errors to affect the encoded information. A logical operator, denoted as $\bar{X}$ or $\bar{Z}$, is an operator that commutes with all stabilizers, yet is not itself in the stabilizer group. In this way, logical operators act on the encoded states within the $+1$-subspace, changing the state of the logical qubit while not being detectable using stabilizer measurements. Effective QEC codes must therefore make it difficult for errors to create a logical operator (logical error). We quantify this difficulty in two ways: code distance and energy barriers.

1. *Code distance*

Operators that act on encoded quantum states are only uniquely defined modulo multiplication by stabilizers. The weight of a logical operator—the number of single-qubit Pauli operators required to construct it—is therefore variable. The code distance is defined as the minimum weight operator that can create a logical error on the code, taking into account this multiplication by stabilizers.

2. *Energy barriers*

Additionally, we can consider the physical qubits in a QEC code as forming a quantum condensed matter system, evolving under a Hamiltonian

$$H = -\sum_{i=1}^{s} S_i, \tag{2}$$

where $\{S_i\}_{i=1}^{s}$ are spatially local operators that generate the stabilizer group $\mathcal{S}$. Since the encoded states belong to the $+1$-eigenspace of all S_i, they also correspond to the ground state (minimum energy state) of this system. Pauli errors then map an encoded state into the -1-eigenspace of some S_i, thus increasing the energy. These *flipped* or *excited* stabilizers can be interpreted as the location of excitations or quasiparticles, with emergent behavior such as mobility, charge, and even braiding statistics. The ability of a code to correct against local errors is equivalent to the condition of *topological order*: The state of the system cannot be determined solely by local operations [7,12,13,39–41].

The energy barrier of this system is then defined as the minimum energy that must be surpassed to create a logical error by sequentially applying single-qubit Pauli errors. Importantly, larger energy barriers will cause the evolution of the system to naturally suppress the creation of logical errors when at nonzero temperatures. That is, for an energy barrier E, entropy change S, temperature T, and Boltzmann constant k_B, the time a system can remain in its encoded state (quantum memory time) scales approximately via the Arrhenius Law [42]

$$\tau_{\text{lifetime}} \sim \exp\left(\frac{E - TS}{k_B T}\right). \tag{3}$$

A *self-correcting quantum memory* at finite temperature is then defined as a QEC code where the lifetime grows without bound in the number of physical qubits, at sufficiently small nonzero temperature [43]. A necessary condition for this, therefore, is that the energy barrier must grow with the system size. However, this behavior is impossible in all stabilizer codes formed by arranging the qubits in $(2+1)$D and demanding the stabilizers be spatially local [8–11,14–18]. These no-go theorems do not necessarily apply to higher dimensions. In particular, self-correction is readily possible in $(4+1)$D [7,15,44]. In $(3+1)$D, there have been several attempts at creating such behavior [8,16,42,43,45–47]. One of the more promising candidates, and one of the only exactly solvable candidates, is known as the *cubic code*.

B. Cubic code

Initially proposed in Ref. [19], the cubic code is defined on a $(3+1)$D simple cubic lattice with two qubits at each lattice site and periodically identified boundaries in all directions, forming a 3-torus. We use the notation XI to denote the operator $X \otimes I$ acting on the two qubits at a particular lattice

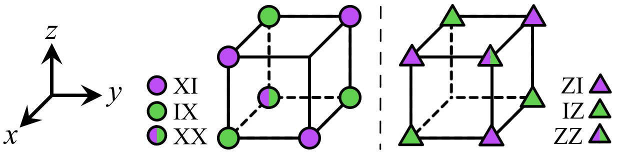

FIG. 1. Generators of the cubic code stabilizers, comprised of single-qubit Pauli operators. (Left) The C_X operator. (Right) The C_Z operator.

TABLE III. The elementary charges of the cubic code. Filled triangles and circles are used throughout this manuscript to refer to the Pauli operators. Color refers to the convention for indicating created charges.

Charge	Created by	Excited stabilizer	Color
e	▲ ZI ▲ IZ ▲ ZZ	C_X	🟩
m	● XI ● IX ● XX	C_Z	🟨

site, with the identity on all other qubits. The model has two kinds of stabilizer generators, both with support on a subset of the 16 qubits at the 8 vertices of a unit cube. These generators, referred to here as C_X and C_Z, are shown in Fig. 1.

Pauli operators create tetrahedral excitation patterns in the neighboring stabilizers, highlighted in Fig. 2. Following the convention with the surface code, we denote these two types of excitations as e and m as in Table III.

1. Lattice symmetries

Noting the form of the stabilizers and their excitation patterns, there are three lattice symmetries of the cubic code relevant for discussions in this paper:

(1) Threefold rotation about $\hat{x}+\hat{y}+\hat{z}$.

(2) Mirror symmetry about the plane normal to $\hat{x}-\hat{y}$.

(3) The map $\{IX \leftrightarrow ZI, IZ \leftrightarrow XI\}$ combined with spatial inversion.

These symmetries are used to relate boundaries and defects with different orientations in later sections.

2. Encoding properties

The defining property of the cubic code is that all its nontrivial topological quasiparticle excitations[1] are fundamentally immobile *fractons*. This is equivalent to a property called “no stringlike operators” [19]. A stringlike operator is any operator that creates two constant-sized regions of nontrivial topological excitations, separated by an arbitrary distance Δ, with a weight that scales linearly with Δ. In doing so, these operators incur a maximum energy cost that is independent of Δ. Since such stringlike operators do not exist in the cubic code, fractons cannot be moved large distances with constant energy. This immobility property is discussed further in Sec. II B 3.

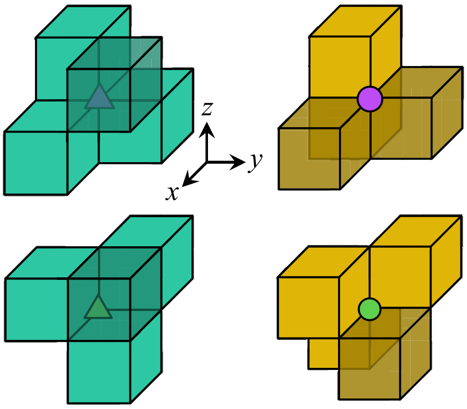

FIG. 2. As per Table III, each single-qubit Pauli operator creates 4 excitations of cubic code stabilizers, arranged in a tetrahedral shape. Transparency is used to show cubes hidden by the 3D perspective.

Importantly, this behavior results in a code distance that scales superlinearly with the linear system size L (the number of sites in each lattice direction), and an energy barrier that scales logarithmically with L. Although seemingly promising for use in self-correction, we also need to consider the effects of entropy. The entropy of a system is typically extensive, scaling polynomially with system size [29]. As per Eq. (3), at finite temperature there will thus exist a given system size where increasing n further results in a decrease to the lifetime, as entropic contributions overwhelm the system. This energy barrier is therefore enough to ensure only *partial self-correction* of the system [48]. Nevertheless, it remains one of the only stabilizer codes to achieve even this behavior.

A key theorem for self-correcting quantum memories is that for there to be no stringlike operators, the ground-state degeneracy—or equivalently, the number of encoded qubits k—in a (3 + 1)D translation-invariant stabilizer code must depend on the system size [16]. In the case of the cubic code, k fluctuates significantly, bounded by $2 \leqslant k \leqslant 4L-2$, where we take a geometry with equal linear system size L in x, y, and z. For notation, we define

$$q_n(L) = \begin{cases} 1 & n|L, \\ 0 & \text{otherwise,} \end{cases} \tag{4}$$

and

$$\zeta(L) = \begin{cases} \max\{2^z \,:\, 2^z|L,\ z \in \mathbb{Z}\} & L \in \mathbb{Z}, \\ 0 & \text{otherwise.} \end{cases} \tag{5}$$

Using this, the exact empirical formula for $2 \leqslant L \leqslant 200$ is given by (see Ref. [19])

$$k = 2[1 - 2q_2 + 2\zeta(L)(q_2 + 12q_{15} + 60q_{63})], \tag{6}$$

where we have written $q_2 = q_2(L)$, etc., for readability. This relationship is plotted in Fig. 3. A number-theoretic exact formula for $k(L)$ is known for all L but the formula is cumbersome to write down and not enlightening for our purposes

[1] A nontrivial topological excitation is one that cannot be created locally.

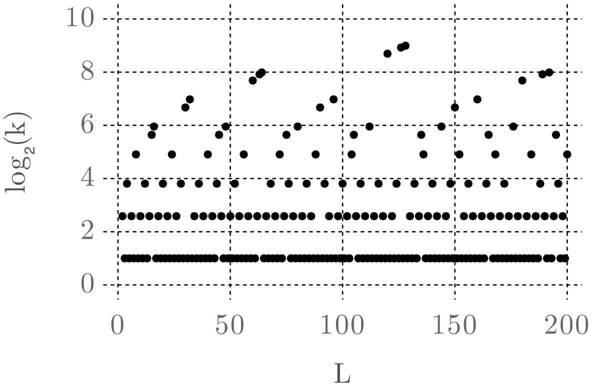

FIG. 3. Number of encoded qubits, k, in the periodic cubic code model with linear system size (L, L, L) in x, y, z, as per Eq. (6). The value is bounded by $2 \leqslant k \leqslant 4L - 2$.

[49]. Importantly, there is a strong dependence on the exact divisibility of L; changing $L \mapsto L + 1$ can cause k to fluctuate by several orders of magnitude. A guiding question for this work is whether the scaling can become a more consistent—ideally linear—function of L by introducing open boundaries and lattice defects.

3. *Fracton mobility*

As noted previously, there are no stringlike operators through the bulk of the cubic code model. Consequently, the topological quasiparticle excitations are strictly immobile and cannot be moved through the lattice without incurring an additional energy penalty that scales with the distance, Δ. There are three sufficient behaviors, presented below, that describe this generalized motion and form the basis of our arguments for code distance and energy barriers in later sections.

4. *Fractal operators*

First, fractons can be moved through the bulk of the model using operators arranged in the shape of *fractal* tetrahedra. Originally described in Ref. [19], the excitation patterns in Fig. 2 can be repeated in a fractal pattern to create increasingly larger separations of charge, as in Fig. 4. Notably, doing so requires multiple excitations to move outwards and it involves intermediary high-energy states. It was from this fractal behavior that the logarithmic energy barrier of the periodic cubic code was derived [29]. Due to this fractal nature, this process can create excitations separated by a distance Δ where $\Delta = 2^j$ for $j = 0, 1, 2, \ldots$. This dependence on powers of 2 contributes towards the sporadic scaling of logical qubits in the periodic cubic code: if the width of the lattice is not a power of 2, multiple smaller tetrahedra need to be combined in a nontrivial way, wrapping around the periodic boundary to annihilate all charges. This motivates the form of Eq. (5).

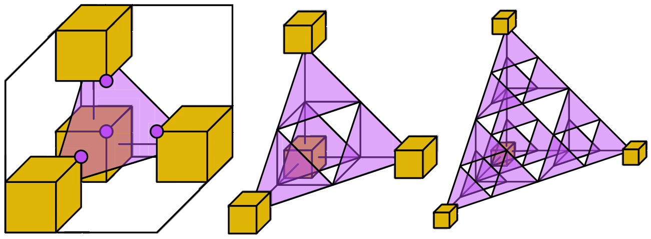

FIG. 4. Fractal pattern used to expand the separation between a set of 4 m excitations in the bulk, using repeated XI Pauli operators (purple circles). The shaded purple regions are used to highlight repeated applications of the leftmost operator, showing similarities to a Sierpinski pyramid.

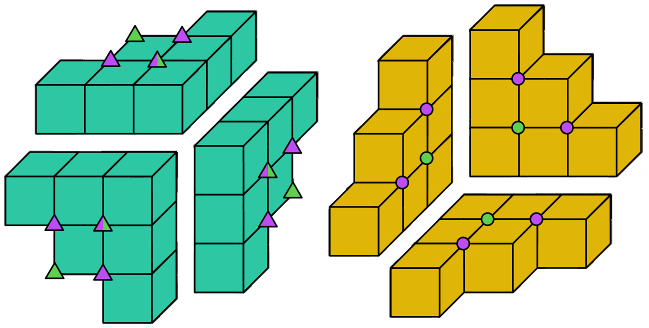

FIG. 5. The F operators that can cascade excitations through the lattice, as in Fig. 6. (Left) F_e^{xy}, F_e^{xz}, and F_e^{yz} operators. The labels indicate the plane and directions along which the excitations can move. (Right) $F_m^{\bar{x}\bar{y}}$, $F_m^{\bar{x}\bar{z}}$, and $F_m^{\bar{y}\bar{z}}$ operators, which move excitations in the negative lattice directions.

5. *Cascade operators*

Second, excitations can be moved in a *cascading* operation (using the terminology from Ref. [32]) that creates additional excitations at each step of the motion. To highlight this, we introduce three operators for e and m, as in Fig. 5. Using these operators repeatedly creates the cascading procedure shown in Fig. 6. Importantly, this process moves excitations through the bulk while requiring a Pauli weight that scales superlinearly with the distance Δ, and creates a number of additional excitations that scales linearly with Δ.

Numerically continuing this process for larger separations produces the results in Fig. 7. This shows the idealized upper bounds for a cascade between two opposing infinite planes. In finite systems, however, cascade operators also provide intuition on the lower bounds for weight and energy costs. While the $\log(L)$ lower-bound on the energy barrier in the bulk is explained by the requirement of nontrivial fractal operators, this does not necessarily hold in settings that break translation-invariance due to the introduction of a defect. We argue in Sec. IV A that the cascade operators instead form an algebra that naturally explains the prevalence of constant energy barriers in certain relevant configurations. Interpreting the form of these logical operators allows us to design systems that circumvent this bound in ways that would not be apparent using only the standard fractal tetrahedral operators.

6. *Cage operators*

Third, following the terminology of Ref. [32], a *cage* operator is a generalization of a Wilson loop that moves excitations around a closed path in the bulk, starting and ending from the vacuum state (ground state). This process is shown in

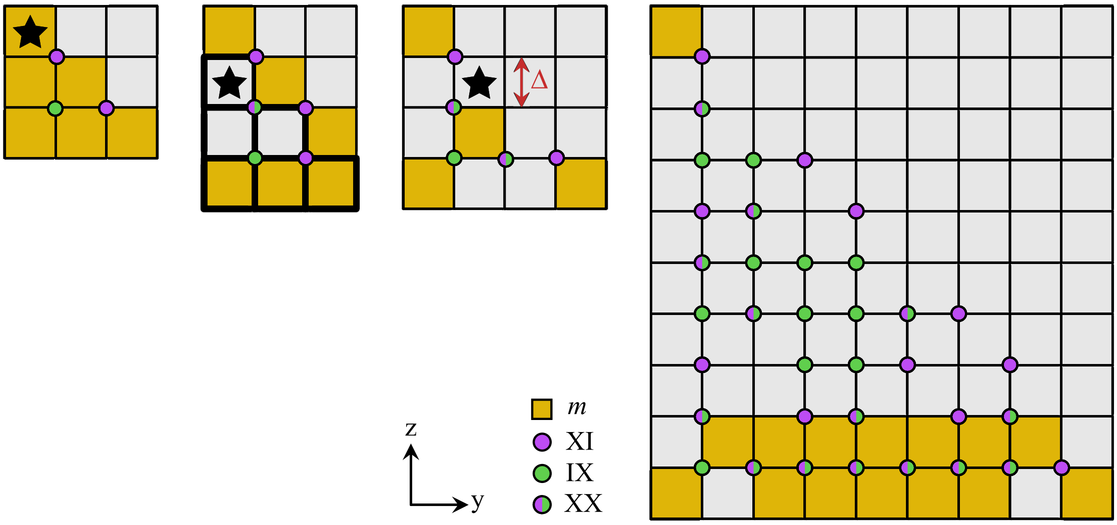

(a) $\Delta = 0$ (b) (c) $\Delta = 1$ (d) $\Delta = 7$

FIG. 6. The "cascading procedure": The $F_m^{\bar{y}\bar{z}}$ operator in panel (a) can move excitations in the $-\hat{z}$ direction. Starting with the excitation pattern in panel (a), we translate and reapply $F_m^{\bar{y}\bar{z}}$ so that the ⋆ is aligned with the ⋆ in panel (b). In doing so, the stabilizers marked by the black squares are flipped. Repeating this at the ⋆ in panel (c) removes all excitations in the second row. We can repeat this process in each row to separate m charges in the $-\hat{z}$ direction. Larger separations Δ create additional excitations and the weight of the operator (number of single-qubit Pauli operators) scales superlinearly with Δ.

Fig. 8. Notably, the locations of Pauli operators, as well as the intermediary excitations, occupy a cylindrical shell with the required height of the cylinder scaling linearly with the radius. When viewed from a particular direction ($\hat{z}$ in Fig. 8), this height can be compacted, leaving a 2D loop. Cage operators are particularly relevant for the discussion of defects in Sec. V.

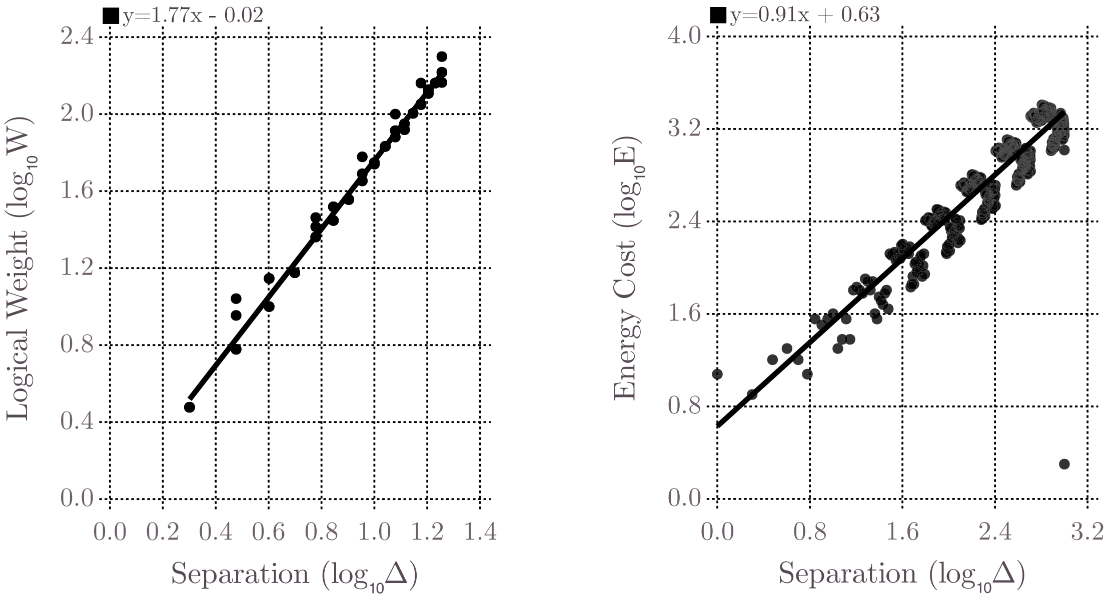

(a) Pauli weight (number of single-qubit Pauli operators) of repeated F operators as the separation between charges (Δ) is increased. A slope of > 1 indicates superlinearity, due to the log-log axes.

(b) Upper bound on the energy cost associated with tunneling a charge between two boundaries. The data point at the bottom right indicates that the excess charges have condensed at the other boundary.

FIG. 7. Scaling properties of the F operators as the separation between charges (Δ) is increased, computed by numerically continuing the process in Fig. 6. This demonstrates a superlinear upper bound on the weight and a near-linear polynomial upper bound on the energy barrier of a logical operator.

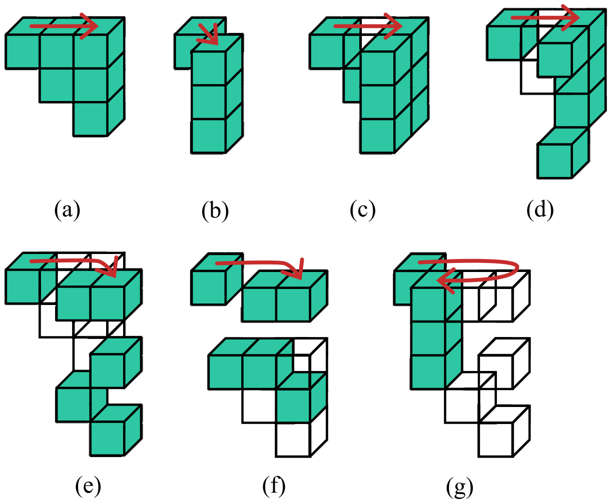

FIG. 8. Using F_e^{yz} and a new operator, G, to move excitations around a closed path ("cage") in the xy plane. (a) The F_e^{yz} operator that we use to move excitations in the $\hat{y}$ direction. (b) A new operator, which we call G (see Fig. 25 in the Appendix), that can be used to move excitations in the $\hat{x}+\hat{y}$ direction. (c) Starting with F_e^{yz}, we move an excitation in the second column into the $\hat{x}+\hat{y}$ direction using the tip of the new operator, G. Wireframe cubes indicate the annihilated charges from the previous step. (d) We then repeat this, using G to move the second excitation in the second column. (e) We now move all three excitations in the third column into the $\hat{x}+\hat{y}$ direction, using G. (f) We now use F_e^{yz} to begin to move these charges back in the $-\hat{y}$ direction. (g) We continue this process to move the remaining charges back in the $-\hat{y}$ direction. To complete the loop, we would use G once again. This process can be generalized to larger loops, in other planes, and also with m charges.

C. Numerical methods

In this work, we aim to derive formulas for the number of encoded qubits, k, and the distance, d, of variants of the cubic code with defects and modified boundary conditions. In general, however, it is difficult to rigorously derive exact equations for these properties. Therefore, we present motivating discussions, backed up by numerical computations of small system sizes where we can determine empirical formulas for these results. We then assume a consistent extrapolation for larger models.

To perform these calculations, the stabilizers in a system of n qubits are represented by a binary vector in $\mathbb{Z}_2^{2n}$, with a 1 corresponding to a Pauli X or Z acting on a particular qubit [50]. Commutation is a bilinear map between two such vectors, and finding nontrivial logical operators reduces to determining the kernel of this map when applied to the stabilizers. In this way, the number of logical operators (or equivalently, the ground-state degeneracy), and also examples of particular logical algebras, can be computed exactly for system sizes up to the order of 20^3 qubits. By restricting to a subset of the physical qubits, we can also determine the properties of the support of these logical operators. These results form the basis for the conclusions drawn in the following sections. Code for these calculations is provided in Appendix C 3.

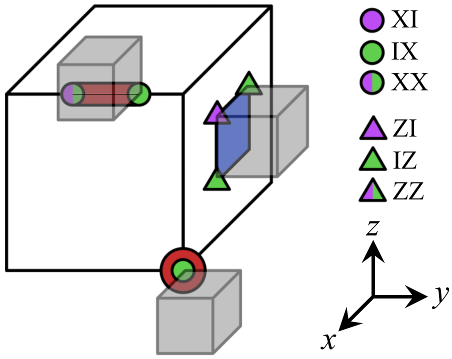

FIG. 9. From top to bottom: Truncated stabilizers on the edges, plaquettes, and vertices of a finite lattice, formed by taking a section of the bulk C_X, C_Z stabilizers.

III. BOUNDARIES

In this section, we present and analyze formulations of the cubic code that incorporate combinations of open and periodic boundaries. By doing so, we identify the behavior of excitations on and near these boundaries, to inform the discussion of encoding properties in Sec. IV. We first consider isolated open boundaries in a semi-infinite system, before combining multiple boundaries via edges and vertices.

To characterize these boundaries, we introduce the following notation: Consider a rectangular prism centered at the origin of a Cartesian $(3+1)$D coordinate system, with the terminating boundaries normal to the axes. In similar notation to Miller indices, we use (100) to denote the boundary that forms across the positive x side of the prism and $(\bar{1}00)$ to denote the boundary on the negative x side. Additionally, define the *sign* of a boundary to be *positive* for (100), (010), and (001) orientations and *negative* for $(\bar{1}00)$, $(0\bar{1}0)$, and $(00\bar{1})$. An additional notation for specifying the types of stabilizers on these boundary faces is introduced in Sec. III B. It is possible to consider other more general boundaries, such as those with Miller index (110). We present one such example in Appendix C 2 but will defer the systematic study of these boundaries to future work.

A. Semi-infinite boundaries

We first consider the family of semi-infinite systems, such as $\mathbb{R}^2 \times (-\infty, 0]$ with a single terminating boundary corresponding to a crystallographic plane, and propose a set of maximal stabilizer generators to populate this boundary. There are two possible constructions of translation-invariant Hamiltonian terms that maintain the required commutation relations with both the neighboring bulk and boundary stabilizers. These correspond to truncated C_X and C_Z operators, as shown in Fig. 9, where the bulk operator is continued outwards and all terms that lie beyond the system boundaries are ignored. We denote these single-face (or plaquette) operators as P_X and P_Z.

Let X-type denote a boundary Hamiltonian consisting of only P_X, and Z-type for P_Z. More general configurations are possible, such as the *triangular* code in Table I, but their

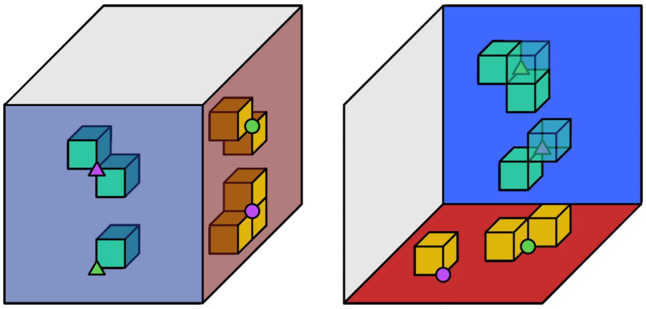

FIG. 10. Positive (left) and negative (right), X-type (red) and Z-type (blue) boundaries, showing the excitation patterns for each combination of single-qubit Pauli operators.

properties can be explained solely by a discussion of the purely X- or Z-type boundaries.

Importantly, the orientation of a boundary affects its behavior. That is, the boundary Hamiltonian of an X-type (001) is not equivalent to that of an X-type $(00\bar{1})$. We see this by observing the two inequivalent forms of truncated C_X, C_Z operators, as well as the symmetries noted in Sec. II B 1.

1. Boundary excitations

Various applications of Pauli operators on a boundary are shown in Fig. 10. When a single particle is able to be created or destroyed in isolation by a local operator in the vicinity of the boundary layer, we refer to this process as *condensation*. Of note, positive Z-type boundaries condense e excitations, while negative X-type boundaries condense m excitations; we refer to these boundaries as (e) and (m) type, respectively. However, on negative Z-type and positive X-type boundaries, single excitations cannot be condensed. Instead, to describe their behavior, we introduce three new charges as subtypes of both the e and m: denoted e_A, e_B, e_C and m_A, m_B, m_C.

Consider a positive X-type boundary in Fig. 11, where we striate the lattice to color squares along the diagonals as A, B, or C (such that an m excitation on an A-type square will have an m_A charge, etc.). Importantly, a single m_A (or an m_A and an m_B, for example) cannot be condensed in isolation. Instead, it gains (2 + 1)D mobility along the boundary plane: m_A charges are mobile along the A diagonals via applications of IX, and can hop to other A diagonals using a combination of IX, XI. Equivalent results hold for m_B and m_C. This increased mobility resembles phenomena observed on the boundaries of type-I fracton models, like the X-cube model [27,32].

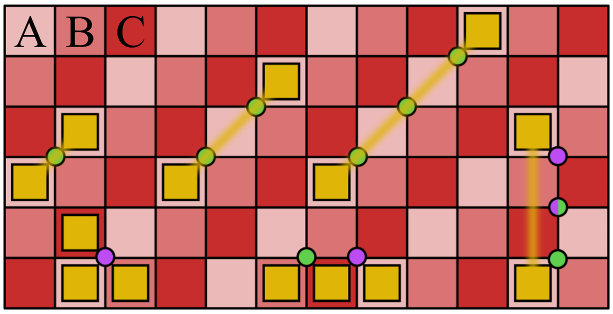

FIG. 11. An X-type positive boundary, colored to indicate three types of m charges: m_A, m_B and m_C. Each charge is mobile within its particular set of diagonals.

TABLE IV. Boundary labels based on the type of topological charge that condenses. Boundary sign is defined as per Sec. III. Color refers to the convention used in the figures.

Boundary	Stabilizer	Sign	Color	Behavior
(m)	X	$-$	🟥	m condenses
(m_{ABC})	X	$+$	🟥	Eq. (7)
(e)	Z	$+$	🟦	e condenses
(e_{ABC})	Z	$-$	🟦	Eq. (7) (for e)

Moreover, XI creates a topologically nontrivial composite of m_A, m_B, and m_C excitations on the boundary. Motivated by these behaviors, we define the fusion rules

$$m_A \times m_A \sim 1,\ \ m_B \times m_B \sim 1,\ \ m_C \times m_C \sim 1,$$
$$m_A \times m_B \times m_C \sim 1 \tag{7}$$

that describe how combinations of excitations can be created via local operators. We note that these are $\mathbb{Z}_2 \times \mathbb{Z}_2$ fusion rules. An analogous result holds for e_A, e_B, and e_C by substituting $m \mapsto e$. Given this fundamentally different behavior to (m) boundaries, we denote these positive X-type boundaries as (m_{ABC}), and similarly (e_{ABC}) for negative Z-type boundaries. A summary of the new boundary notation is given in Table IV.

For these charges to be considered topologically distinct, there must not be a local operator that can fuse $m_A \times m_B \sim 1$, for example. By considering the action of IX and XI, this is trivially true using only operators with support on the boundary. Since such a fusion operator will create excitations only along the boundary, we complete the argument by using the cleaning process from Refs. [19,51] to reduce the support of any bulk operator to just terms on the boundary; we refer the reader there for a more detailed description. This argument holds when we consider operators stretching from the (m_{ABC}) boundary into the bulk, as long as the operator does not have support on other boundaries [such as an opposing (m)]. Therefore, it is valid to consider m_A, m_B, and m_C as distinct charges with the boundary fusion properties above, if they are separated from additional boundaries by distances larger than the correlation length of the ground state.

Due to the triplet $\mathbb{Z}_2 \times \mathbb{Z}_2$ fusion nature of these charges, these fusion rules bear a resemblance to that of the *color code* [34,52,53]. In fact, the color code can be directly transformed into this (2 + 1)D layer: Consider the hexagonal lattice of the 6-6-6 color code in Fig. 12, with a qubit at each lattice point (white circle). The stabilizers of this code are the product of X or Z on all 6 qubits of each hexagon. We begin the transformation by first overlaying a rhomboidal lattice such that its vertices lie between exactly two qubits i, j, as shown in the inset. Note that acting on both qubits with X_iX_j, for example, excites the two adjacent stabilizers on the green hexagons. This is equivalent to exciting two A squares along the diagonal of the cubic code's (m_{ABC}) using IX in Fig. 11. Moreover, acting with just X_iI_j excites the three adjacent red, green, and blue hexagons—equivalent to exciting m_A, m_B, and

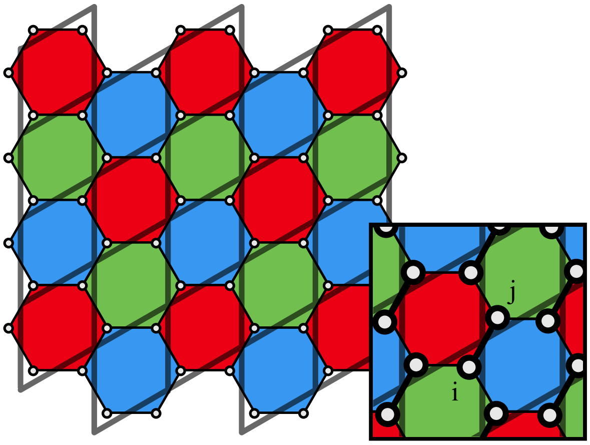

FIG. 12. A hexagonal color code, with a qubit at each white circle. Overlayed is a rhomboidal lattice, with vertices corresponding to the lattice points in the boundary layer of the cubic code. As per the inset, at each vertex the adjacent two color code qubits i, j are identified with the two qubits at each cubic code lattice site. To map onto the cubic code stabilizers a CNOT is used on each pair, controlled on qubit j.

m_C using XI on the cubic code. Corresponding similarities also apply for Z operators acting on an (e_{ABC}) boundary. We, therefore, have the following map relating excitations of the color code to excitations of the cubic code boundaries:

$$X_iX_j \mapsto IX,\ X_iI_j \mapsto XI,\ Z_iZ_j \mapsto ZI,\ I_iZ_j \mapsto IZ. \quad (8)$$

Notably, in the Heisenberg representation this transformation is equivalent to acting on each i, j pair with a CNOT gate, controlled on qubit j [38]. If we consider the (m_{ABC}) boundary on (100) and (e_{ABC}) on $(\bar{1}00)$, then this transformation directly maps the truncated boundary X and Z stabilizers of the cubic code onto the X and Z stabilizers of the color code. This property is discussed further in Appendix C 2. It remains an open question as to how or whether this correspondence generalizes to the bulk stabilizers of the cubic code, and moreover for the other cubic codes proposed by Haah [19].

2. *Periodic behavior*

Consider a lattice that is periodic in $x, y \in [0, L]$ and occupies $z \in [0, \infty)$. Along the $(00\bar{1})$ face we construct an (e_{ABC}) boundary using P_Z stabilizers. If $3|L$, then the diagonal striation (as in Fig. 11) of this boundary layer is self-consistent and we have distinct e_A, e_B, and e_C charges that are mobile within their $(2+1)$D diagonal subspaces. That is, if an e_A were to move around the periodic boundary, then it would retain its e_A charge. We can thus consider an operator that creates two e_A out of the vacuum, hops one around the periodic boundary, and annihilates it with the other to create a logical operator—comparable to those in the $(2+1)$D toric code, for example, [5]. Due to the two unique charges (as $A \times B \sim C$ by the fusion rules), these surface string operators define two independent logical operators along an (e_{ABC}) or (m_{ABC}) boundary. When $3 \nmid L$, it can be checked that hopping an excitation three times around a boundary (to return it to its original labeling) produces the identity operator.

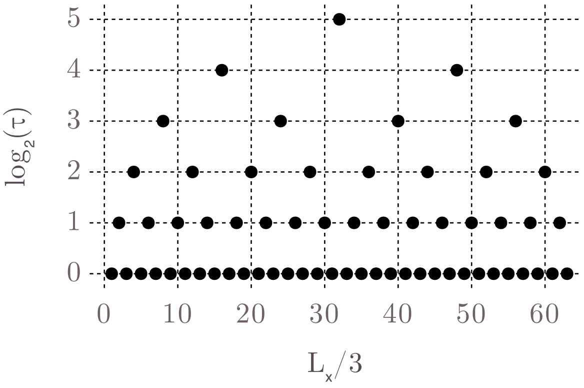

FIG. 13. Numerical calculation of $\tau(L_x, L_\infty) \equiv \zeta(L_x/3)$ from Eq. (5) for increasing linear system sizes L_x with $L_\infty \gg L_x$. There is a clear fractal nature to this behavior.

However, these string operators can be extended to additional layers beyond the boundary, creating operators that extend into the bulk while requiring longer periods. To describe this procedure, we consider each xy plane to be a generalization of the boundary (e_{ABC}) layer. That is, acting with IZ or ZI at $z = 1$ creates e_{ABC} charges in both the $z = 0$ and $z = 1$ layers. Repeating the hopping process at $z = 1$ to move an e_A around the periodic boundary will remove all charges in that layer while introducing *residual* charge at $z = 0$. If this residual charge is *trivial*—that is, it is equivalent to the vacuum state up to the fusion operators in Eq. (7)—then the charge in that layer can also be cleaned away. Importantly, these processes only deposit residual charge in layers at smaller z, not affecting layers that have already been cleaned of excitations. Since (e_{ABC}) restricts any remaining charge from forming beyond the $(00\bar{1})$ face itself, completing the process by annihilating charges at $z = 0$ results in a (nontrivial) logical operator.

If this process were started instead at $z > 1$, then this cleaning can be continued downwards until either the topmost remaining layer has a nontrivial residual charge or all charges are annihilated or condensed into the (e_{ABC}) boundary. In this way, nontrivial logical operators can be constructed at varying depths within the bulk, which wrap around the periodic boundary and iteratively clean layers of charge down to $z = 0$.

It can be shown (see Appendix C 1) that for a given lattice that is periodic in linear system size L, the maximum number of z layers that can be cleaned until a nontrivial residual charge is created is

$$z_{\max}(L) = \zeta(L/3) \quad (9)$$

using the notation in Eq. (5). This function is plotted in Fig. 13. Each layer introduces two additional nontrivial mutually commuting logical operators, giving

$$k = 2\zeta(L/3). \quad (10)$$

Note that if $L_z < z_{\max}(L)$ and the (001) boundary is of type (m) or (m_{ABC}), then $k = 2L_z$ since the maximum number of layers cannot fit in the given lattice. Incorporating this, we define the function

$$\tau(L_1;\ L_2) = \min\{\zeta(L_1/3),\ L_2\}. \quad (11)$$

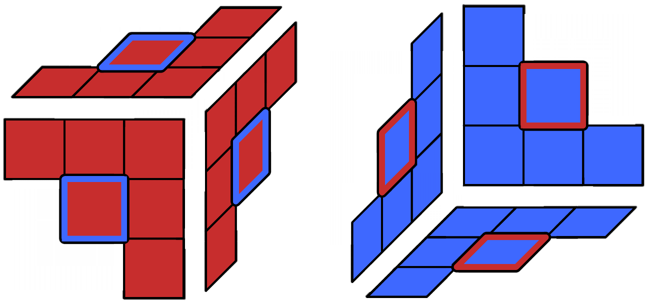

FIG. 14. Anticommutation relations for plaquette operators on the boundary. (Left) When P_Z is applied to the blue square on the positive faces of the lattice, the red squares on the same face correspond to P_X that anticommute. (Right) When P_X is applied to the red square on the negative faces of the lattice, the blue squares correspond to P_Z that anticommute.

For rectangular lattices with $L_x \neq L_y$, then we instead have

$$k = 2\min\{\tau(L_x;\ L_z),\ \tau(L_y;\ L_z)\} \tag{12}$$

defined by the shortest path around the periodic boundary. As a result, $k = 0$ if one of L_x or L_y is not a multiple of 3.

3. *Translational-symmetry violations*

If translational invariance is relaxed, then there are additional possible commuting configurations of the boundary Hamiltonian. The commutation relation between neighboring plaquette terms is given in Fig 14. Notably, these relations allow for the construction of a natural *diagonal* commuting interface between P_X, P_Z operators, such as the configuration labeled *triangular* in Table I.

As with the other boundaries discussed so far, each sector of the mixed boundary is associated with an (e), (m), (e_{ABC}), or (m_{ABC}) behavior. Due to this equivalence, this paper focuses on pure X and Z boundary configurations.

B. Boundary seams

As in Fig. 9, two adjacent boundaries can be joined along an edge, and three boundaries at a vertex. These features are required to construct the full codes discussed in Sec. IV.

Notably, the plaquette-plaquette commutation relations in Fig. 14 are equivalent for edge-plaquette commutation since geometrically, neighboring plaquettes only share support on at most two sites—identical to plaquettes. Given these constraints, we can thus specify a fully gapped configuration for a finite prism such as in Table I. To describe these configurations, the notation $(xyz;\bar{x}\bar{y}\bar{z})$ is used to specify the boundary type on each of the six lattice boundaries (see Fig. 15). For open boundaries, we use e and m as defined in Table IV, where the ABC subscript is dropped for readability. Periodic boundaries are denoted by p. It is assumed in each case that the edge and vertex stabilizers are chosen to create a maximally commuting stabilizer group of local operators (that is, where possible there are no local Pauli operators with support on a single plaquette, edge, or vertex that commute with all the stabilizers).

Using this notation, we can revisit the symmetries described in Sec. II B 1:

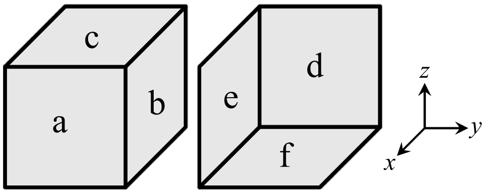

FIG. 15. Notation used to specify the choice of boundaries, $(abc;def)$, where each letter is e or m (as defined in Table IV and the ABC subscript is implied), or p for a periodic boundary.

(1) $(abc;def)$ is equivalent to $(cab;fde)$ and $(bca;efd)$.
(2) $(abc;def)$ is equivalent to $(bac;edf)$.
(3) $(abc;def)$ is equivalent to $(def;abc)$ with all $e \leftrightarrow m$ swapped.

Combined, the first two symmetries imply that for $(abc;def)$, all permutations of abc produce equivalent codes, given that the same permutation is also applied to def.

IV. BOUNDARY CODES

A core motivation for this work is to maintain the partial self-correction of the cubic code, without the requirement of nonlocality to implement a 3-torus. Given the discussion in Sec. II, operators with superlinear weight (necessary for self-correction) arise when excitations *cascade* through the bulk of the lattice, while unwanted stringlike operators appear near certain boundary configurations. Motivated by this, we thus consider codes that contain opposing (e), (e_{ABC}) boundaries and opposing (m), (m_{ABC}) boundaries. This specifies four of the six faces of the lattice, leaving (up to symmetries) a potential three unique configurations. In the following section, we highlight one such case, dubbed *tennis ball 1*, while the others are discussed in Appendix A.

A. Tennis ball 1

This configuration is constructed with (e_{ABC}) and (m_{ABC}) on the remaining two unspecified faces. For example, $(mem;mee)$ as shown in Table I.

To construct $\bar{X}$ logical operators, m charges must cascade from (100) and condense at $(\bar{1}00)$ using $F_m^{\bar{x}\bar{y}}$ and $F_m^{\bar{x}\bar{z}}$, as shown in Fig. 16. If the m excitations produced in the cascade cannot appear on the (001) boundary, then this procedure produces an operator with a weight superlinear in L_x and an increasing energy barrier, since excitations must cascade through the bulk by a distance L_x. However, if m excitations *can* be produced on the (001) boundary during the cascade, then these excitations become mobile on the surface and can hop to the $(\bar{1}00)$ face using a string operator. Hence, any cascade that begins less than a distance of order $\mathcal{O}(L_x)$ from the (001) boundary creates a stringlike operator: the height is constant in L_x, the weight is linear, and the energy cost is constant. An analogous argument holds for producing $\bar{Z}$ logical operators by cascading e excitations; only cascades which begin a distance at least $\simeq L_y$ from the $(00\bar{1})$ boundary produce logical operators with superlinear weight.

Notably, the $\bar{X}$ logical operators extend in the $\hat{z}$ direction and $\bar{Z}$ in the $-\hat{z}$ direction when cascading. Pairs of $\bar{X}$ and $\bar{Z}$ must then anticommute along their shared xy-plane. To

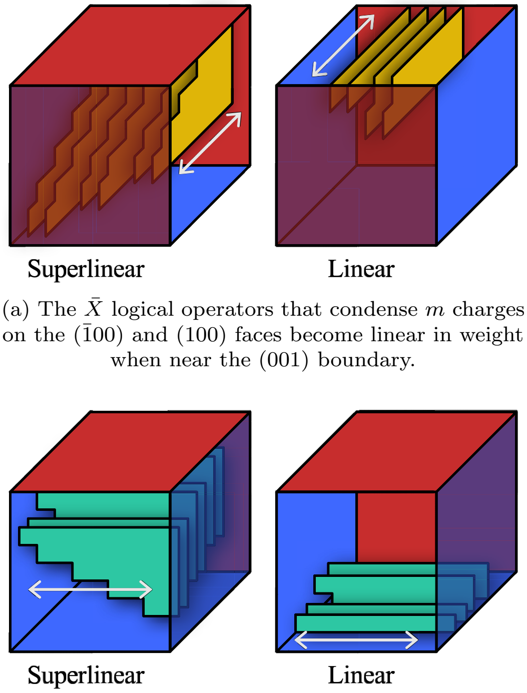

(a) The $\bar{X}$ logical operators that condense m charges on the $(\bar{1}00)$ and (100) faces become linear in weight when near the (001) boundary.

(b) The $\bar{Z}$ logical operators that condense e charges on the $(0\bar{1}0)$ and (010) faces become linear in weight when near the $(00\bar{1})$ boundary.

FIG. 16. Logical operators on the first *tennis ball* configuration, (*mem*; *mee*). Solid shapes indicate repeated applications of the F operators to cascade m (yellow) and e (cyan) charges. Red faces represent X, and blue for Z, stabilizer choices on the boundaries.

determine the number of independent logical pairs, first note that using the *long* edge of the F operators to move charges through the bulk is equivalent to the hopping operator in Fig. 11. We can then identify this cascading procedure with hopping an A, B, or C charge from one boundary to the other, creating neighboring intermediary excitations that must also be hopped into a condensing boundary. In a similar argument to Sec. III A 2, we, therefore, expect each layer to contribute 2 encoded qubits. Since only one orientation, namely, the xy planes, have opposing e and m-condensing boundaries—and therefore can support mutually anticommuting pairs of both e and m operators—the scaling is thus expected to be $k = 2L_z$. We confirm this by numerically computing the ground-state degeneracy for small values of L_x, L_y, L_z; an example of the computed logical algebra cleaned into a single xy plane is shown in Fig. 17. This same analysis cannot be conducted with xz planes, for example, since these will have three adjoining m-type boundaries and only one e-type. As with the surface code, such a configuration does not support any nontrivial logical operators.

Notably, this scaling confirms the results in Ref. [54], where Dua et al. showed that the periodic cubic code can be interpreted as interwoven layers of toric code. Specifically, a model of linear system size (L_x, L_y, L_z) is equivalent to $2L_z$ copies of toric code, up to a unitary that is nonlocal in z. When placed on open boundaries as done here, the corresponding surface codes should each contain one encoded qubit, thus giving $k = 2L_z$ total.

B. Subsystem codes

The presence of the stringlike operators initially appears detrimental to the desired self-correcting behavior of the *tennis ball* code. However, we can still ensure a superlinear-distance encoding by using a subsystem code [55]. By treating all logical qubits with linear distance as gauge qubits, the subsequent dressed logical operators should remain superlinear in weight. We argue this claim as follows:

First, note that the support of the bare superlinear-weight logical operators extends further in the z direction than the bare linear-weight logical operators, by definition. This extra support includes a region in the bulk where the $\bar{X}$ and $\bar{Z}$ pairs intersect and anticommute. Since $\bar{X}$ commutes with all stabilizers and all other $\bar{Z}$ operators apart from its pair, this anticommutation relation must be maintained when multiplied with these other operators. Therefore, the product of bare superlinear and bare linear weight operators will always contain support on a region in the bulk of the lattice. This region is either entirely isolated from the boundary or extends to the boundary. In the former case, by the properties of the original cubic code, there are no stringlike operators in the bulk of the lattice. For the latter, the operator now occupies a support that is larger than the original superlinear-weight support, which didn't extend to the boundary. In both situations, the dressed operator must still have superlinear weight.

With *tennis ball 1*, we can, for example, label all logical operators that can be supported solely in $z \geqslant 2L_z/3$ or $z \leqslant L_z/3$ as ancillary. Computing the remaining ground-state degeneracy numerically, the number of logical qubits is

$$k = 2\left(\left\lfloor \frac{L_z}{3} \right\rfloor + (L_z \bmod 3)\right). \tag{13}$$

The periodic scaling is a result of specifying discrete lattice points for the cutoff regions when 3 may not divide L_z.

It is therefore possible to modify the family of cubic codes such that we maintain the superlinear distance and partial self-correction while improving k to be a simple linear function of L_i, with only a constant-order periodic correction. Moreover, these codes do not require any periodic boundaries and are thus comparably more realistic for implementations in physical systems.

V. DEFECTS

Having presented the key properties of boundaries in the cubic code in the previous section, in the following section we similarly introduce and characterize three defect types: vacancies, edge dislocations, and screw dislocations. A discussion of their use in QEC codes is then provided in Sec. VI. Defects have been used in previous work to encode additional quantum information and to perform logical Clifford operations [30,31,53,56–60].

From a condensed matter perspective, defects are an important consideration when forming a complete understanding of a given phase of matter. For example, encircling a defect can induce a lattice translation. Since fractons are fundamentally immobile, this translation has the potential to cause nontrivial changes to the fracton topological order [61], such as in the form of increased mobility.

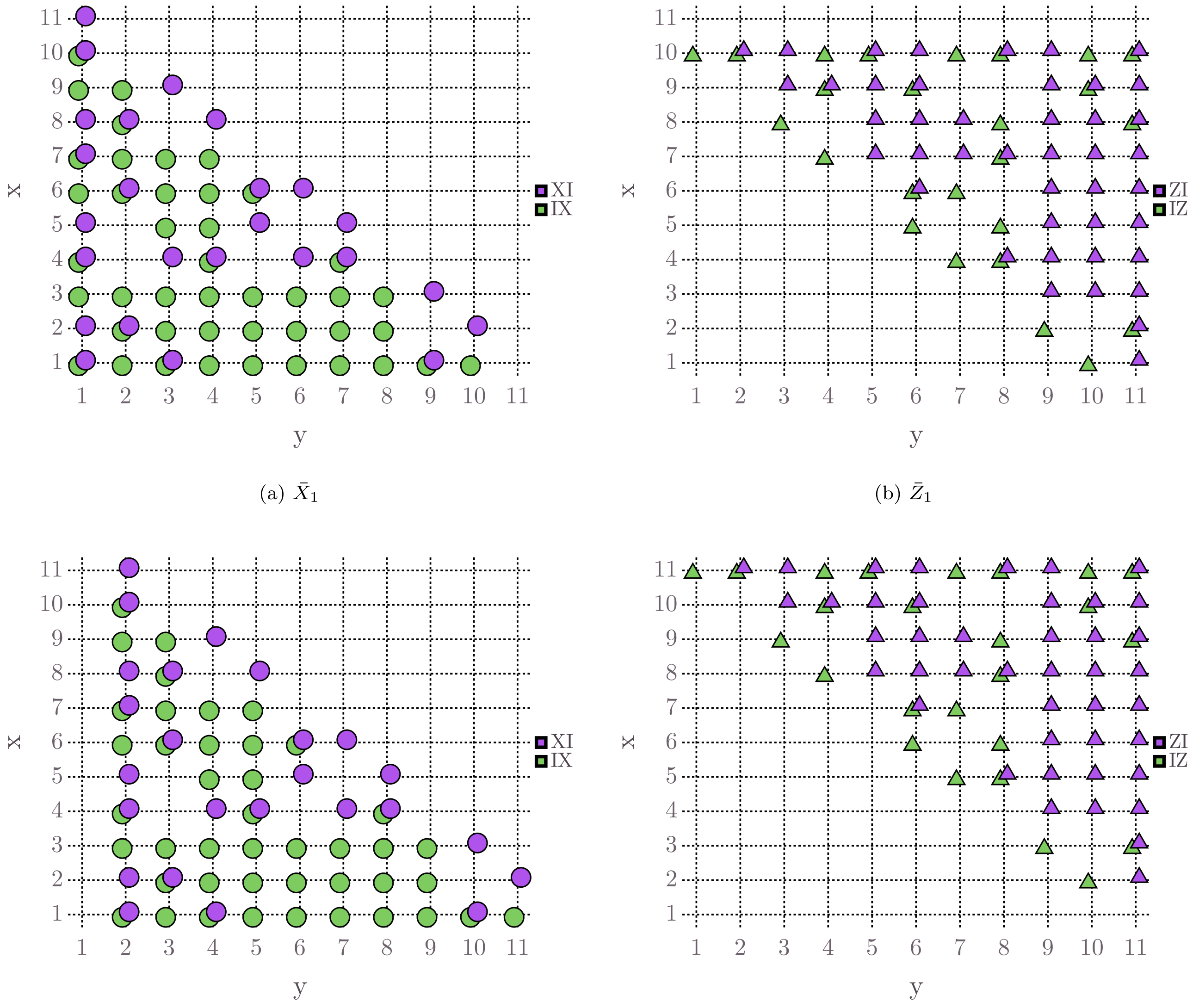

(a) $\bar{X}_1$

(b) $\bar{Z}_1$

(c) $\bar{X}_2$

(d) $\bar{Z}_2$

FIG. 17. Two pairs of logical operators on the first *tennis ball* code (*mem*; *mee*), for a linear system size $(11, 11, L_z)$, considering a slice of the xy plane at some z far from the (001) and $(00\bar{1})$ boundaries. These were calculated and plotted computationally; a slight jitter is applied to each point to distinguish when XI and IX occur on the same lattice point. Note that there are only two such pairs of logical operators that can be cleaned onto just this particular xy plane. If we consider the plane at $z + 1$, then we would find an analogous result of two new independent pairs of logical operators; in this way, the *tennis ball 1* code has $k = 2L_z$ logical pairs.

A. Vacancies

Vacancies, the removal of lattice sites (and qubits) within the bulk of the model, behave similarly to boundaries. Stabilizers obtained by truncating the operators acting on the vacant site still commute with all stabilizers away from the vacancy and with other truncated stabilizers of the same type. Indeed, as per Ref. [62], it is always possible to construct a set of local commuting terms to gap the 1D boundary of a translation-invariant Pauli stabilizer model in 2D. We are not aware of an analogous result that characterizes the form of the boundary algebra in more general cases. For simplicity, we consider only vacancies with single choices of truncated stabilizers, which we denote as $\langle m\rangle$ and $\langle e\rangle$ for X and Z, respectively. As with the boundaries, these results could be generalized to more complex constructions, such as (110) orientations, isolating only one of the qubits at a given lattice sites, or constructing combinations of e and m faces, in future works.

We identify here three key ways in which bulk excitations interact with nearby vacancies, the first two of which are equivalent to the boundary interactions.

First, fractons can condense into certain faces of $\langle m\rangle$ and $\langle e\rangle$ vacancies, just as with the exterior lattice boundaries. The analogous results to Table IV are summarized in Table V.

Second, if the vacancy extends in a particular direction, such as $\hat{z}$, then mobilized charges on (m_{ABC}) and (e_{ABC}) faces of the vacancy are able to repeatedly *hop* along $\hat{z}$. If the vacancy extends around a lattice periodic in z, and with $3|L_z$,

TABLE V. Terminology for vacancies, analogous to Table IV for open boundaries.

Vacancy type	Vacancy boundary	Stabilizer	Boundary sign	Behavior
$\langle m\rangle$	(m)	X	$+$	m condenses
$\langle m\rangle$	(m_{ABC})	X	$-$	Eq. (7)
$\langle e\rangle$	(e)	Z	$-$	e condenses
$\langle e\rangle$	(e_{ABC})	Z	$+$	Eq. (7) (for e)

then an operator can create two m_A out of the vacuum, hop one charge around the periodic boundary and annihilate it with the other. This is equivalent to the boundary behavior in Sec. III A 2.

Finally, by employing a *cage operator*, fractons can encircle a vacancy. As described in Ref. [32] and Sec. II B 6, these operators create a set of fractons out of the vacuum, separate them via a cascading procedure in two directions, before inverting the cascading operation to bring the excitations back together to annihilate—returning to the vacuum state. Such an operation in the bulk will typically be trivial, resulting in a product of stabilizers. However, the vacancy removes terms from the stabilizer group, causing a cage that encircles a vacancy to be potentially nontrivial.

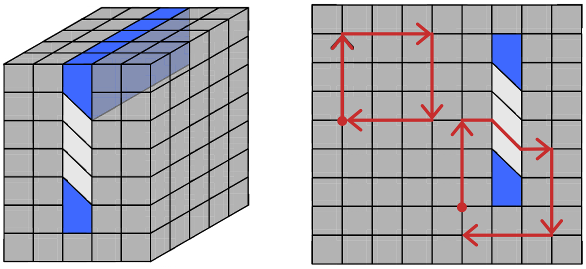

(a) At the ends of the dislocation are two *twist* stabilizer lines (blue), shaped like trapezoidal prisms.

(b) Closed loops in the bulk and around a twist.

FIG. 18. Edge dislocations on the cubic code contain twists (blue). An operator that moves a fracton around a closed cage (red loop) in the bulk will no longer be closed when encircling a twist. This translation potentially increases the mobility of fractons when near a defect.

B. Edge dislocations

Edge dislocations in (3 + 1)D are analogous to those in the (2 + 1)D surface code [30], with the additional feature that the dislocation becomes a line extending into the third spatial dimension, as in Fig. 18. Along the dislocation line, we include trapezoidal prism stabilizer terms—known as *twists* in Refs. [30,56]. Joining the twists are a region of slanted C_X and C_Z operators (shown as white in Fig. 18) that naturally commute with the adjoining bulk stabilizers. For the twists themselves, however, there are only two choices of stabilizers: one from X terms (denoted T_X) and another from Z (T_Z). These are provided in Fig. 19. Importantly, although T_X and T_Z commute at the same location, adjacent T_X and T_Z anticommute. Constructing a gapped edge dislocation, therefore, requires taking either pure T_X, pure T_Z, or T_X and T_Z jointly on every second stabilizer (or some combination of the above). We could further consider a noncommuting, potentially gapless, Hamiltonian along the defect including all T_X and T_Z terms with arbitrary weights. Due to the commutation relations, this Hamiltonian is seen to be equivalent to two copies of the (1 + 1)D quantum Ising model. We proceed to consider only the pure T_X or T_Z defects, leaving more complicated configurations to future work.

As sketched in Fig. 18(b), using a cage operator to propagate a fracton around a twist does not return the fracton to its original position; instead, the fracton moves by the Burgers vector of the dislocation. The once-immobile fractons thus gain limited mobility in the vicinity of a twist. This behavior has the potential to introduce nontrivial logical operators.

As with boundaries and vacancies, bulk excitations can condense onto particular twists. A T_X twist condenses m charges, while T_Z twist condenses e. Since an edge dislocation is characterized by two twists, we denote, for example, $\langle em\rangle$ to be a T_X twist on the positive side of the pair, and T_Z on the negative side.

C. Screw dislocations

The final defect type we consider is the *screw dislocation*, shown in Fig. 20. We label the screw as $\langle L\rangle$ or $\langle R\rangle$ by the handedness of the Burgers vector when traversing around the

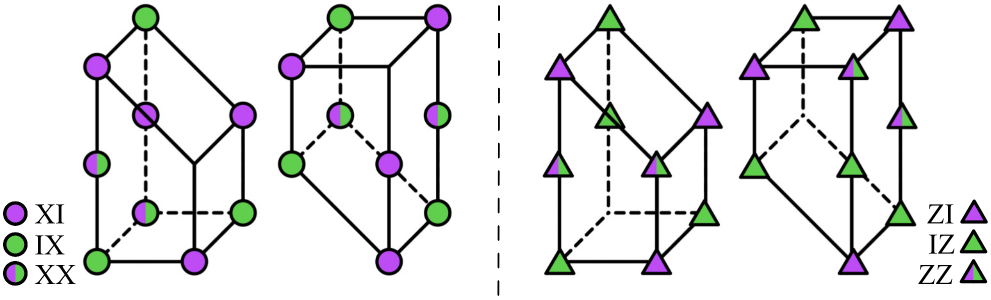

FIG. 19. Stabilizers for the twists occurring at the ends of edge dislocations. There are four types, corresponding to T_X (left pane) and T_Z (right pane), as well as at the bottom and top of the edge dislocation. The stabilizers were found by considering the commutation with the neighboring bulk C_X and C_Z stabilizers.

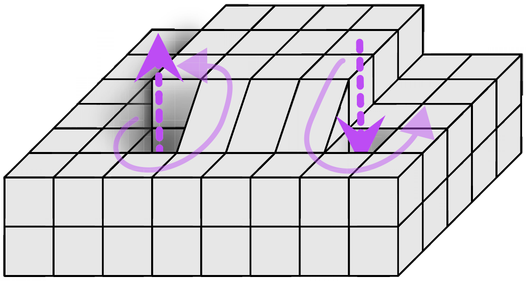

FIG. 20. The two independent forms of screw dislocations in a (3 + 1)D lattice, such as the cubic code. The screws are labeled by the handedness of the Burgers vector when traversing around the dislocation. On the left is a right-handed screw, $\langle R\rangle$, and on the right is a left-handed screw, $\langle L\rangle$.

dislocation. Unlike the edge dislocation, the screw invokes a translation vector along the defect line itself. Importantly, this means that a fracton can continuously wind around the defect via cage operators while translating along the screw. Fractons thus gain 1D mobility in the vicinity of screw dislocations.

Unlike vacancies and twists, however, for the screw dislocations with a Burgers vector of 1 considered here, there is no local operator supported on the dislocation line that commutes with the bulk stabilizers. Because of this, $\langle L\rangle$ and $\langle R\rangle$ screws have no inherent stabilizer and can condense both m and e excitations. Notably, this condensation behavior largely negates any change to the mobility of fractons near this screw, since individual e and m can be created or destroyed at any location along the defect, and thus become trivial.

VI. DEFECT CODES

Similar to the discussion of boundary codes in Sec. IV, in this section we examine how defects can be used with the cubic code to create QEC codes with superlinear distances. Further configurations without this property are discussed in Appendix B. Notably, although there are codes using screw dislocations with a superlinear distance, the number of encoded qubits there is constant. We therefore defer the discussion of screw-dislocation codes to Appendix B 3.

A. Vacancy encodings

Consider a lattice of size $(L_x, L_y, L_z) = (L_\infty, L_\infty, L_z)$, where $L_\infty \gg L_z, \kappa$ with κ the correlation length of the ground state, such that interactions with the x, y boundaries are negligible. We also place periodic boundary conditions in the z direction. Within this, there is an $\langle m\rangle$ vacancy of width (w_x, w_y, L_z) such that it extends around the periodic boundary. We expect that a single vacancy in this configuration does not modify the ground-state degeneracy, since creating and annihilating m on the same vacancy is trivial. Indeed, this result is confirmed by numerical computation, in all cases except when $3|L_z$. As discussed in Sec. III A 2, m charges gain 1D mobility along a periodic boundary, producing additional logical operators. This gives a number of encoded qubits,

$$k = 4\tau(L_z;\ L_\infty), \tag{14}$$

where τ is defined in Eq. (11), with the factor of 4 arising from the two unique stringlike operators on the two (m_{ABC}) boundaries of the vacancy. These logical operators all have a linear weight.

Once additional $\langle m\rangle$ vacancies are introduced, however, additional logical operators arise. Numerically computing the ground-state degeneracies, the number of encoded qubits scales with

$$k = 2(v-1)L_z + 4\tau(L_z;\ L_\infty), \tag{15}$$

where v is the number of vacancies.

m excitations can now cascade through the bulk from one vacancy to another, creating an $\bar{X}$ logical operator with a weight that is superlinear in the vacancy separation Δ (using the Manhattan distance). Each additional vacancy introduces an additional independent site for condensation, thus increasing k. Moreover, since translation is a nontrivial action in the bulk of the model, performing the cascading procedure at different values of z produces independent operators. This gives the dependence on L_z.

However, the $\bar{Z}$ logical operators are formed from cages of e excitations encircling a vacancy. Importantly, because these cage operators are moving charges through the bulk around the vacancy, these must also have a weight that scales superlinearly with the widths w_x, w_y. If these widths were scaled with the separation between the vacancies, then this encoding has the potential to be partially self-correcting (when $3\nmid L_z$), while also supporting a number of encoded qubits that scale linearly in L_z and the number of vacancies.

If the assumption of $L_x, L_y \gg L_z$ is relaxed, such as for an $(mmp; mmp)$ code with v number of $\langle m\rangle$ vacancies wrapping around the periodic boundary, then we get two additional logical operators per L_z, giving

$$k = 2vL_z + 4\tau(L_z;\ L_\infty) \tag{16}$$

in comparison to Eq. (15). This is because m charges can now also cascade from the vacancies to a boundary.

Overall, this code is a notable improvement over the original cubic code model and does not require a subsystem code as in Sec. IV. Unlike vacancies in the surface code, there is also no significant tradeoff between the code distance and the number of encoded qubits, since v can be kept constant while using L_z to increase k, and using the x, y dimensions (vacancy width and linear system size) to increase the code distance. However, this construction does require a topology with one periodic direction.

B. Edge dislocation encodings

A single edge dislocation in the bulk, far from any boundary, encodes no additional logical qubits.

However, more appealing behavior arises using multiple edge dislocations. Consider two dislocations, in Fig. 21(a), each of height h in the z direction and separated by perpendicular distance Δ in the y direction. The dislocation line extends along x. Numerically computing the ground space degeneracy yields

$$k = 4L_x + \mathcal{O}(1) \tag{17}$$

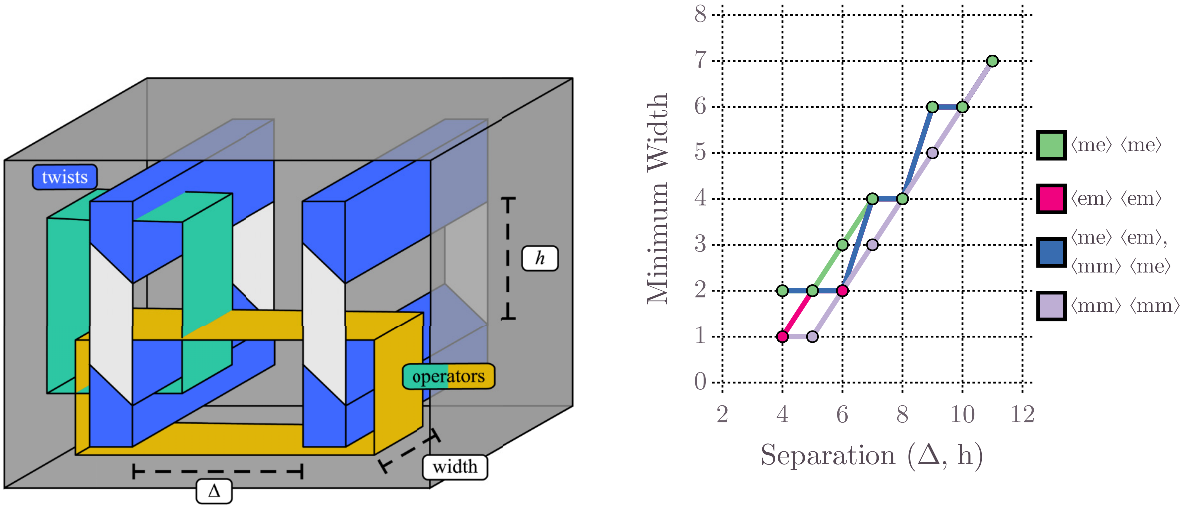

(a) Logical operators between pairs of $\langle mm\rangle$ twists. One traverses the gap between two twists on the same dislocation, while the other joins one twist from each pair. The coloring in this picture was arbitrary: e and m operators can be found in both configurations.

(b) Minimum x width required to support at least one logical operator, as the height h and separation Δ increases. Colors show results for different twist types. A linearly-increasing width indicates that the weight of the operator should be superlinear in $\Delta = h$.

FIG. 21. Pairs of edge dislocations support superlinear-weight logical operators.

for some additional constant arising depending on the exact choice of twist stabilizers, Δ, and h.

Effectively, these logical operators consist of movement of e and m excitations around and between two of the four twists, as in Fig. 21(a). Importantly, because these cage operators are moving charges through the bulk, the prohibition of stringlike operators means that the width of the support in the x direction must increase with h and Δ. This result is confirmed by numerically computing the minimum width that supports logical operators as we scale $\Delta = h$ in Fig. 21(b). Slight variations in the widths are due to the particulars for constructing the operators around the twists. However, in all cases, we observe an overall linear trend.

If the analysis above is repeated except with open or periodic boundary conditions in x, then we observe the same scaling as in Eq. (17). There is an additional, constant number of logical operators that have support solely on a single twist and are stringlike in the x direction. Unlike the case with vacancies, these operators remain even if $3 \nmid L_x$. As with the case for *tennis ball 1*, considering a subsystem code to ignore these extra logical operators may be sufficient to ensure the dressed code has a superlinear distance as Δ and h are increased. A rigorous proof of this solution is deferred to future works.

As with periodic vacancies, pairs of twists provide a promising approach to improve the cubic code: maintaining the desirable code distance while encoding a number of qubits that scales linearly with L_x.

VII. CONCLUSION

In this work, we have presented a systematic study of open boundaries and defects in Haah's cubic code. We focused on planar (100)-like boundaries normal to the crystallographic axes and constructed X- and Z-type open boundary conditions using truncated plaquette, edge and vertex stabilizer terms. The interaction of these boundaries with fractonic topological excitations depends intrinsically on their orientation: X-type negative faces and Z-type positive faces condense single fractons of the respective type, while the opposing faces lead to increased fracton mobility within their vicinity. These otherwise fractonic excitations become mobile within a $(2+1)$D diagonal subsystem along the surface. This implies that the fundamental no-stringlike-operator property of the original cubic code is violated in the vicinity of these boundaries.

Similar behavior was observed in the vicinity of vacancies, edge dislocations, and screw dislocations: patterns of fracton condensation that lead to increased mobility were seen to depend on the orientation and stabilizer type of each defect. The nontrivial action of translation symmetry on a type-II fracton topological phase means that encircling a dislocation defect with a cage operator can also lead to increased topological excitation mobility. We found that dislocation defect encodings were therefore able to support additional forms of logical operators that do not appear for encodings constructed from boundaries and vacancies.

The cubic code is known to form a partially self-correcting quantum memory on periodic boundary conditions [48]. The absence of any stringlike logical operator is essential to enable such a quantum memory [19]. With this in mind, we aimed to determine if it is possible to retain the superlinear distance of the original cubic code model while making the number of encoded qubits scale as a simple linear function of the linear system size, without sporadic fluctuation. We have shown that it is possible to achieve this using a combination of open and periodic boundaries, vacancies, and defects, despite the no-stringlike-operator property potentially being lost when translation-invariance is violated by the introduction of defects. For cubic codes with open boundary conditions—which are typically easier to realize in a physical implementation—it is possible to achieve a superlinear code distance by restricting the encoded states to a subsystem, with all dressed logical operators maintaining a weight that scales superlinearly with the linear system size. We have shown this to be possible with the *tennis ball 1* code construction. It is an open question whether this can be generalized to other open boundary condition codes, such as those in Appendix A. Our results also focused on planar (100)-like boundaries; it remains an open question as to whether alternate constructions such as (110) boundaries yield fundamentally different behavior.

We showed that emergent $(2+1)$D topological order arises on certain open boundary conditions, supporting particles with increased mobility. Interestingly, this phase can be unitarily transformed into the 6-6-6 color code. We leave a further investigation of this correspondence, such as how it extends into the bulk, to future research. Similarly, it would be interesting to relate the bulk cubic code defects to defects of the color code [53] on the boundary. Presumably, the emergent color code on the boundary has an associated noninvertible anomaly [63] which is a property of the type-II fracton bulk phase. Understanding the nature of the surface topological order could uncover further insights into type-II fracton topological order via a bulk-boundary correspondence.

In this work we have only explored Pauli-X or Z type boundaries of the cubic code, rather than more complicated mixed or twisted boundary conditions. We suspect that such boundary conditions exist and are inequivalent to those we have studied. Our reasoning uses the construction of twisted boundaries via gauging symmetry-protected topological (SPT) domain walls [64]. For the cubic code, this allows a construction of boundaries via the gauging duality to a 3D fractal Ising model [27,28]. For one type of boundary condition of the fractal Ising model, the symmetry action on the boundary is simply the action of the bulk fractal symmetry restricted to the boundary plane. This symmetry action on the boundary appears to also be a fractal of the form considered in Ref. [65]. Following Ref. [65], one can consider stacking the fractal Ising model with a reflected copy of itself such that the resulting boundary fractal symmetry supports a nontrivial fractal SPT phase. We can then twist the boundary condition by the associated SPT entangler and gauge the resulting model to obtain a twisted boundary condition of a cubic code stacked with a reflected cubic code. We leave the detailed study and classification of such twisted boundary conditions to future work. We anticipate that existing constructions of type-II fracton models from layers of fractal SPTs may prove advantageous for this study [66].

We now highlight several further directions for future consideration. It remains to be seen how the results in this paper can be generalized to other type-II fracton topological phases, such as the additional codes introduced in Ref. [19] or the fractal spin liquid codes [25]. It would be interesting to relate defects in the latter codes to known defects in $(2+1)$D topological codes via the fractalization procedure of Ref. [67]. Our work, together with previous work on type-I fracton phases [32,33], raises the question of developing a general theory of boundaries and defects for fracton topological orders. A promising approach to this is the inclusion of conventional topological boundaries and defects into the topological defect network framework for fracton topological order [68–70]. Another interesting open question is the development of a notion of Lagrangian algebra objects [71–74] for fracton topological orders that can be used to classify possible gapped boundaries in relation to fracton braiding statistics [75,76]. A further challenge is the extension of these concepts to non-Abelian fracton models [77–84].

Our work leaves open the question of superlinear code distances for subspace stabilizer encodings in type-II codes with open boundary conditions. It could be interesting to search for bounds on the best achievable parameters for a topological subspace stabilizer code with open boundary conditions in $(3+1)$D. Proving rigorous lower bounds on the code distance and energy barriers, as well as modifying the decoding algorithms from Refs. [20,85] in the presence of boundaries and defects, would allow us to make a more definitive judgment on the feasibility of these codes as self-correcting quantum memories. It would also be useful to consider how lattice defects can be braided to produce Clifford gate sets, such as with the surface code [30]. Another open direction for future work is calculating the fusion of multiple twist and screw dislocations to create defects with larger Burgers vectors, and the relationship between braiding and condensations on these defects. This raises the challenge of developing a theory of translation symmetry enrichment for fracton topological orders, extending the $(2+1)$D results of Ref. [57]. This is a promising lens through which to understand the general structure of fracton topological orders on crystal lattices. We remark that the possible phenomena exhibited by known fracton models reveal a far richer theory than the two-dimensional analog [86]. In particular, a general theory should capture the interplay between subgroups of translation symmetry and bifurcating entanglement-renormalization group flows satisfied by fracton topological orders including the cubic code [87–90].

All numerical evaluations were performed using Julia, the code for which can be found at Ref. [91].

ACKNOWLEDGMENTS

The authors acknowledge fruitful collaboration with Tom Iadecola and Meng Cheng during the early stages of this work. A.D. and D.B. are supported by the Simons Collaboration on Ultra-Quantum Matter, which is a grant from the Simons Foundation (Grant No. 651438, A.D.; Grant No. 651440, D.B.). A.D. is also supported by the Institute for Quantum Information and Matter, an NSF Physics Frontiers Center (Grant No. PHY-1733907). A.C.D. is supported by the Australian Research Council Centre of Excellence for Engineered Quantum Systems (EQUS, Grant No. CE170100009). D.W. is supported by the Australian Research Council Discovery Early Career Research Award (Grant No. DE220100625).

APPENDIX A: ADDITIONAL BOUNDARY CODES

Configurations such as *tennis ball 1*, vacancies around periodic boundaries, and pairs of twists have the potential to be partially self-correcting, while having a number of encoded qubits that scales linearly in some macroscopic quantity. However, this behavior is not true for the majority of other configurations. In this section, we present the remaining results from a systematic study of all boundary configurations (up to symmetries, and with pure (100)-like planar boundaries). A discussion on defects is provided in Appendix B.

We first consider models with open boundary conditions on all six faces, before also addressing combinations with periodic boundaries. We perform a systematic search over all configurations, up to symmetries, and their key results are summarized in Tables I and II.

1. Simple cases

Following the construction in Sec. III, we first verify that our boundary conditions produce gapped surface Hamiltonians. To do so, we construct an (L_x, L_y, L_z) model with only X or Z stabilizers on all faces: $(eee; eee)$ or $(mmm; mmm)$. Numerically, we verify that all configurations (tested up to reasonable lattice sizes) contain a nondegenerate ground state—or equivalently, no encoded qubits. Intuitively, this agrees with our analysis so far. Consider $(mmm; mmm)$. Using either the cascading procedure or the fractal tetrahedra, one can consider m excitations moving between two or more opposing boundaries of the lattice, creating an operator that commutes with the stabilizers. However, no product of Z operators can create and annihilate e excitations to produce a nontrivial $\bar{Z}$ logical operator. There are thus no encoded logical qubits and an equivalent argument holds for $(eee; eee)$.

For similar reasons, if one face is replaced with the opposing boundary type, such as $(mmm; emm)$, then we again see no encoded logical qubits. As with other stabilizer codes, creating an excitation on a boundary and then condensing it back into the same boundary does not constitute a nontrivial operation [6].

2. Tennis ball 2

In addition to the first *tennis ball* code discussed in Sec. IV A, there are two additional configurations that we argued may have a superlinear distance. The second *tennis ball* code is specified using (e) and (m) on the remaining two faces. Consider the case shown in Table I, with $(mee; mem)$.

The logical operators can be constructed by a similar cascading procedure to *tennis ball 1*, except now acting along a diagonal direction (see Fig. 22). As with the first *tennis ball*, not all such logical operators are superlinear. Indeed, those localized near the $(\bar{1}\bar{1}0)$ and (011) edges are constant-weight with respect to the linear system size. That is, as L_x, L_y, L_z are increased, there will remain a number of logical operators with constant support, localized near those edges.

Numerically computing the ground-state degeneracy, we arrive at a number of encoded qubits

$$k = 2L_z - 6, \tag{A1}$$

with the constant offset in comparison to *tennis ball 1* due to the inclusion of vertex stabilizer terms, which would otherwise be incorporated as local logical operators. Note that the analysis here can also be generalized to explain the scaling of encoded qubits for $(eee; mem)$ and $(eee; mmm)$ in Table I (the latter of which has a logical algebra constructed from two independent sets of these diagonal operators).

As with *tennis ball 1*, this code, therefore, does not generally have a superlinear distance. However, it may be possible to generalize the arguments for the subsystem code to also reduce these logical operators into superlinear-weight dressed operators. The specifics of this approach are left as a future consideration.

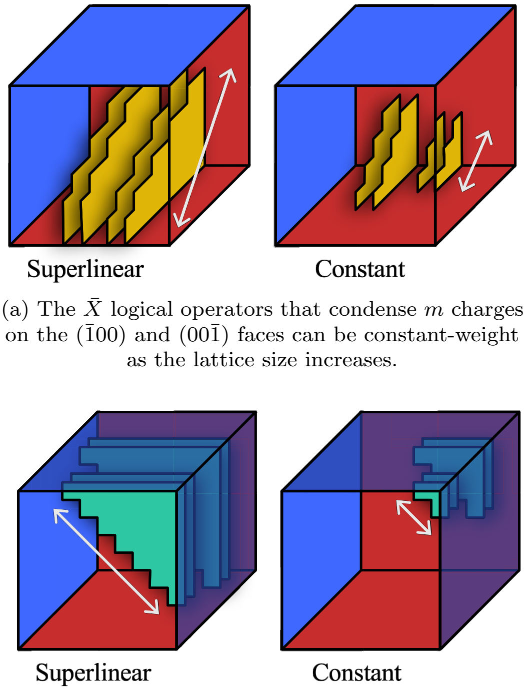

(a) The $\bar{X}$ logical operators that condense m charges on the $(\bar{1}00)$ and $(00\bar{1})$ faces can be constant-weight as the lattice size increases.

(b) The $\bar{Z}$ logical operators that condense e charges on the (010) and (001) faces can also be constant-weight as the lattice size increases.

FIG. 22. Logical operators on the second *tennis ball* configuration, $(mee; mem)$. Solid shapes indicate repeated applications of the F operators to cascade m (yellow) and e (cyan) charges. Red faces represent X, and blue for Z, stabilizer choices on the boundaries.

3. Tube

The third code, *tube*, is specified with (e) and (e_{ABC})—or equivalently, (m) and (m_{ABC})—on the remaining two faces. In Table I, we have chosen $(mee; mee)$.

The $\bar{X}$ logical operators must cascade m charges between the (m) and (m_{ABC}) boundaries, as these are the only possible condensation sites. Such a cascading procedure must incur a superlinear weight as it moves through the bulk of the lattice. Unlike with the *tennis ball* configurations, there is no adjacent (m_{ABC}) face on which the cascade can be cut off, and there are thus no linear-weight operators for $\bar{X}$. However, e charges can move as strings along the (e_{ABC}) boundary of $(00\bar{1})$ as in *tennis ball 1*, and can also form local operators between the (e) boundaries of (010) and (001) as in *tennis ball 2*. This configuration, therefore, improves the $\bar{X}$ distance while reducing the distance for $\bar{Z}$ errors.

Numerically computing the ground-state degeneracy for small system sizes yields a number of encoded qubits

$$k = 2(L_y + L_z - L_x) - 3. \tag{A2}$$

We can heuristically explain this by considering the cascading of m charges from (100) to $(\bar{1}00)$. Using $F_m^{\bar{x}\bar{y}}$, we can create m

on (100) and push them in the $-\hat{x}$ direction. Since the support of the operator increases in width with distance, the maximum distance that the charge can be pushed is L_y before the operator encounters an (e) boundary, beyond which it is confined. Using $F_m^{\bar{x}\bar{z}}$, the accumulated charges can be cascaded a further L_z distance towards $(\bar{1}00)$. If $L_x > L_y + L_z$, then we should get no logical operators. For each $L_x < L_y + L_z$, we expect two additional independent logical operators, accounting for the two unique condensation operators. The constant factor of 3 again arises due to the particular choice of edge and vertex stabilizers on the boundary seams.

4. Periodic boundaries

There are further configurations possible that include mixtures of periodic and open boundary conditions. All possible combinations, up to symmetry, are summarized in Table II.

As discussed in Sec. II and Ref. [20], the ground-state degeneracy of $(ppp; ppp)$ is highly dependent on the specific value of L. This is because the logical operators are formed from combinations of fractal tetrahedra with excitations at the four vertices. When L is a power of 2, these tetrahedra tessellate perfectly and the number of encoded qubits scales as $k = 4L - 2$. For other values of L, the tetrahedra need to be combined in particular ways, possibly wrapping around the periodic boundaries multiple times, leading to a nontrivial function for k, as defined in Eq. (6).

For $(ppe; ppe)$, these tetrahedral operators in Z remain as logical operators, condensing e at the open boundaries or in a similar process to $(ppp; ppp)$. However, the tetrahedra from X create m excitations that cannot condense at the open boundaries, and thus these operators are no longer logical. This reduces the number of encoded qubits by a factor of 2 compared to $(ppp; ppp)$. Additionally, the periodic behavior described in Sec. III A 2 now applies, resulting in additional logical operators when $3|L$. This leads to a scaling

$$k = \tfrac{1}{2}k_{(ppp;ppp)} + 2\tau(L;\ \infty) \qquad \text{(A3)}$$

when $L_x = L_y = L$. Because the e excitations can condense at both boundaries in z, and the periodic behavior is unaffected by L_z, this scaling only depends on L_x, L_y. Note that the string operators on $(00\bar{1})$ are not confined by the (001) face, since e excitations are able to condense there, hence the τ scaling is also unbounded by L_z.

In the case of $(ppm; ppe)$ boundaries, single m or e excitations are not condensed at either boundary, and we have (m_{ABC}) and (e_{ABC}) on (001) and $(00\bar{1})$, respectively. The logical operators here are described by the discussion in Sec. III A 2, and this process can occur on both $(00\bar{1})$ and (001), giving twice as many. For $(pmm; pem)$, a similar behavior occurs, with string operators on the (e_{ABC}) face of $(00\bar{1})$ wrapping around the periodic-x boundary.

However, for $(ppe; ppm)$ there are no encoded logical operators. Neither the (001) (e) boundary nor the $(00\bar{1})$ (m) boundary support string operators.

Finally, $(pem; pem)$ can be explained using the cascading procedure. As with $(mem; eem)$—a rotation of the *tennis ball 1* configuration in Sec. IV such that z becomes x—there are $k = 2L_x$ encoded qubits. Indeed, the logical operators here are equivalent: excitations are created at (e_{ABC}) or (m_{ABC}), and cascade towards (e) or (m) where they are condensed. These operators can be confined to single yz planes, leading to the linear dependence on L_x. The periodic boundaries in x do not impede or alter this process. However, when $3|L_x$, some of these operators can be written as strings across the (e_{ABC}) and (m_{ABC}) boundaries. We therefore get $4\tau(L_x;\ \infty) \leqslant 4L_x/3$ number of linear-weight operators, leaving a minimum of $2L_x/3$ superlinear-weight operators. To avoid this behavior or the need for a subsystem code, linear system size can be restricted to $3\nmid L_x$. In such cases, since the cascading operators form a complete logical algebra and no further linear or constant-weight operators are introduced, we, therefore, expect $(pem; pem)$ to be a stabilizer code with distance that is superlinear in L_y, L_z.

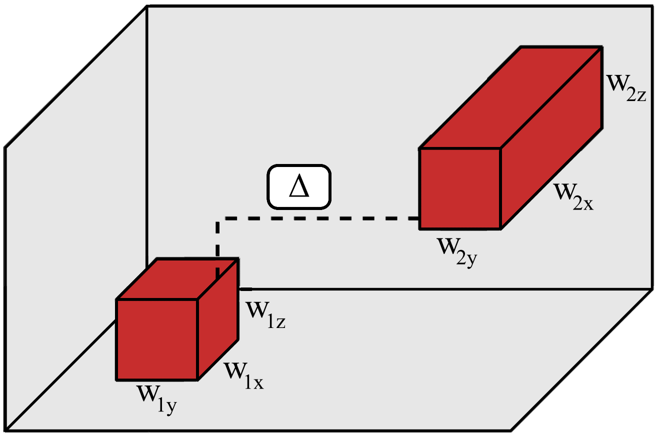

FIG. 23. Two $\langle m\rangle$ vacancies of size (w_{ix}, w_{iy}, w_{iz}) for $i = 1, 2$ separated by a Manhattan distance Δ in the bulk.

APPENDIX B: ADDITIONAL DEFECT CODES

We now present the remaining results regarding the use of vacancies and dislocations in the bulk, adding to the discussions in Sec. VI.

1. Additional vacancy encodings

We now examine codes that incorporate vacancies into both a bulk model and those involving boundaries. Consider a nonperiodic lattice with $L_\infty \gg \kappa$ in x, y, z, where κ is the correlation length of the system such that any interaction with boundary conditions can be deemed negligible. One $\langle m\rangle$ or $\langle e\rangle$ vacancy of any size does not support any logical operators, since any action that creates and condenses charges on the same vacancy is trivial modulo the stabilizers. This is consistent with results from the surface code [30,92].

A similar result is found with one $\langle m\rangle$ and one $\langle e\rangle$ vacancy separated in the bulk, since no excitation can condense at both vacancies.

However, consider two $\langle m\rangle$ vacancies, each of width (w_{ix}, w_{iy}, w_{iz}) where $i = 1, 2$, separated by a Manhattan distance Δ. This is shown in Fig. 23. m excitations can cascade in the negative direction, moving between the two vacancies. Since cascading produces additional excitations proportional to the distance traversed, we expect this procedure to be a logical operator only if the negative vacancy is large enough to

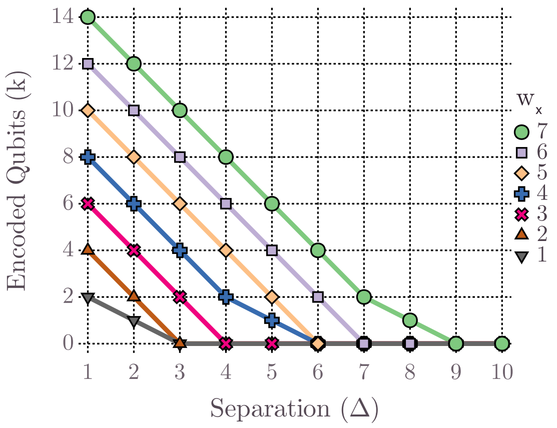

FIG. 24. Numerical computation of the encoded qubits in a pair of $\langle m\rangle$ vacancies oriented along the z direction, separated by distance Δ. The vacancy in the negative direction has size $(w_{1x}, w_{1y}, w_{1z}) = (w_x, 1, 1)$, where w_x is varied in the figure, and the positive vacancy has (1,1,1). We see the relationship in Eq. (B1), with the slight deviations when $w_x = 1, 4, 7$ due to the nonuniformity of composing F_m operators.

condense these excitations. Without loss of generality, assume the two vacancies are separated in z, with $i = 1$ being in the negative direction. We thus have the condition that $k > 0$ only if $\Delta \lesssim w_{1x} + w_{1y}$.

Numerically computing the ground-state degeneracy confirms this result, and provides a number of encoded qubits

$$k = 2(w_{1x} + w_{1y} - \Delta) + c, \tag{B1}$$

where

$$c = \begin{cases} 1 & [3\,|\,(1 + w_{1x} + w_{1y})] \;\cap\; [w_{1x} + w_{1y} = \Delta], \\ 0 & \text{otherwise}, \end{cases} \tag{B2}$$

as shown in Fig. 24. Here, c is a correction factor arising when composing F_m operators results in a deviation to the distance reached for a given width.

Note that the positive vacancy widths do not affect the scaling, since it only needs one lattice point to condense the tip of the cascading operators. The opposite result holds for $\langle e\rangle$ vacancies, where w_2 affects the scaling, rather than w_1.

These cascading operators give a form for the $\bar{X}$ logical operators. However, $\bar{Z}$ logical operators are expected to be formed from moving e charges around the $\langle m\rangle$ vacancy itself, similar to the periodic case. Unlike those vacancies, however, many of these cage operators can be cleaned onto a pyramidal region near the $\hat{x} + \hat{y} + \hat{z}$ vertex of the vacancy and therefore will be local and constant-weight, independent of (w_{ix}, w_{iy}, w_{iz}). This is problematic for the construction of a superlinear-distance error correction code, and it is nontrivial to determine if a subsystem approach is sufficient to create superlinear-weight dressed logical operators. Crucially, the existing lemmas rely on bulk properties that no longer hold in the vicinity of a defect, and so this remains an open question for future research. It, therefore, appears that periodic vacancies provide a more suitable method for improving k while maintaining the partial self-correction properties.

2. Additional edge dislocation encodings

As mentioned, a single edge dislocation (a pair of twists) in the bulk far from any boundaries do not increase the ground-state degeneracy. On periodic boundary conditions (such that the dislocation line extends around the periodic direction), the stringlike operators seen in other configurations emerge when $3|L$.

However, there are additional linear-weight operators. Consider a $\langle ee\rangle$ dislocation extending in the x direction. Acting on one trapezoidal prism in the twist with the T_X operator creates excitations in the neighboring T_Z stabilizers by nature of their anticommutation. By repeating T_X on every second trapezoidal prism, these excitations can move along the defect line. Therefore, if $2|L_x$, then these excitations can wrap around the periodic boundary and annihilate. There are two such operators that do this, depending on the starting position. If L_x is not a multiple of 2, then these excitations can wrap around the periodic boundary twice, annihilating again. In this case, there is only one unique operator: the product of T_X on all trapezoidal prisms.

Although the period-3 strings are independent when constructed on either of the two e twists, these new operators formed on either twist are equivalent modulo stabilizers. Therefore, combining these two behaviors we get a scaling of

$$k = 8\tau(L_x;\ L) + \begin{cases} 2 & 2|L_x, \\ 1 & \text{otherwise}, \end{cases} \tag{B3}$$

where L is the appropriate linear system size to confine the stringlike operators. An equivalent result also holds for $\langle mm\rangle$. For mixed twists $\langle me\rangle$, $\langle em\rangle$, the factor of 2, 1 does not appear since the corresponding anticommuting logical operator spans the separation between the two twists, which must therefore both be of the same type.

3. Screw dislocation encodings

A single $\langle R\rangle$ or $\langle L\rangle$ screw situated far from any boundary has no logical operators. When extending around a periodic boundary, the period-3 strings are present. Since both e and m can condense on a screw dislocation due to the lack of any stabilizer terms, we get twice as large a contribution to the number of encoded qubits per screw. For one screw extending in the z direction, we get

$$k = 4\tau(L_z;\ L_\infty). \tag{B4}$$

For multiple screws, we first consider the case when the net Burgers vector is zero. That is, we have one $\langle L\rangle$ and one $\langle R\rangle$ separated by a Manhattan distance Δ. Computing the ground-state degeneracy, we find the number of encoded qubits to be

$$k = 4\tau(L_z;\ L_\infty) + 2q_2(\Delta), \tag{B5}$$

using the function q from Eq. (4). Unlike edge dislocations, we thus have a number of additional encoded qubits independent of the system size. Heuristically, this is linked to the idea that the action of the screw dislocation introduces mobility along the defect. Spatially translated operators are now no longer necessarily independent. Since these additional logical operators are spanning the bulk between the two screws,

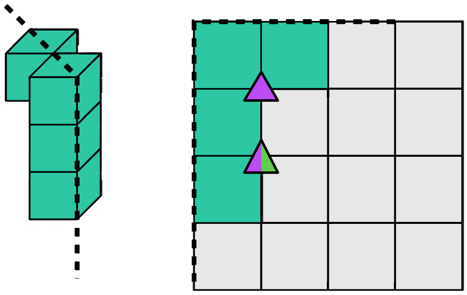

FIG. 25. The operator G, constructed out of IZ and ZZ terms, which moves e excitations along a line. In this representation, creating two e_A in the top layer, for example, will also create an e_A in the second and third layers. Considering the plane indicated by the dashed lines as a 2D grid of just the A diagonal gives the representation on the right, where each square corresponds to a location along that diagonal. This representation is used in Fig. 26.

we expect this configuration to have a superlinear distance, scaling with Δ. However, the constant k value means that these encodings are not ideal candidates in our search for improvements to the cubic code. Although k could be increased by potentially introducing additional screws, this runs into a similar problem observed in the surface code: increasing the weight involves increasing the separation between screws while increasing k involves increasing the number of screws. Achieving both simultaneously results in the system size increasing significantly [14].

From a physical perspective, a nonzero Burgers vector would have a macroscopic effect on the bulk of the material, rather than just on a localized region, and is thus unlikely to be created in isolation [93]. Nevertheless, we can still consider the effect of two $\langle R\rangle$ or $\langle L\rangle$ screws in the bulk. In this case, the formula is

$$k = 4\left\lfloor \frac{L_z - 1}{2} \right\rfloor + 4\tau(L_z;\ L_\infty) + 2q_2(\Delta), \tag{B6}$$

gaining an additional set of logical operators that increases in number with L_z.

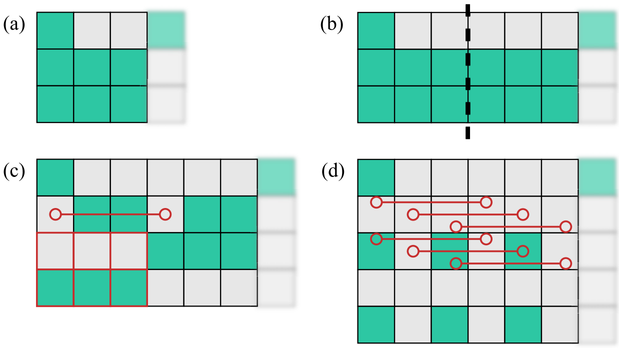

FIG. 26. (a) Repeating the operator in Fig. 25 three times produces this excitation pattern. The resulting operator is named O_3. If the first and fourth columns are identified via a periodic boundary, then this commutes with all stabilizers in the first row. (b) Repeating the operator in panel (a) twice produces this excitation pattern, with a period of 6. (c) Applying O_3 onto the square indicated by the leftmost red circle annihilates two charges in the second layer, while flipping the squares indicated by the red outline. (d) Applying O_3 to each of the 6 charges to the left of the dashed line in panel (b) produces an excitation pattern that is equivalent to (a) but scaled by a factor of 2. This resulting operator is called O_6.

APPENDIX C: ADDITIONAL MATERIAL

1. Proof of Eq. (9)

We first note the following lemma:

Lemma 1. Let P be a local set of (X or Z) Pauli operators with nontrivial excitations occurring on the dual lattice sites S, with $|S| > 1$. Choose an arbitrary site $s \in S$ to be the "anchor" of P. Define the new operator P' by: for each $s_i \in S$, apply the operator P, translated so that the anchor point acts on s_i. Then, the pattern of excitations created by P' is the pattern created by P, scaled by a factor of 2 in all directions.

We now present the proof of Eq. (9):

Proof. First, consider the case where $3\nmid L$. Here, the coloring of A, B, C is not consistent across the periodic boundary. An operator that moves e_A across the boundary will transmute it into an e_B, for example. Repeating this will transmute e_B into an e_C. Applying it a final time will return e_C back into e_A, annihilating with the original charge. However, $e_A \times e_B \times e_C \sim 1$, and hence we have effectively moved a trivial charge around the boundary—therefore producing a trivial operator. This gives $z_{\max}(L) = 0$ when $3\nmid L$ as required.

We now demonstrate the arguments for $L = 3, 6, 9$, before generalizing these results to arbitrary L.

Consider $L = 3$. We employ the operator G, first shown in Fig. 8, drawn into a 2D plane as in Fig. 25 such that all excitations are only of type e_A.

Translating by 1 to the right and reapplying G two more times creates the pattern in Fig. 26(a). Identifying the first and fourth columns via periodic boundary conditions produces an operator that commutes with all stabilizers in the topmost

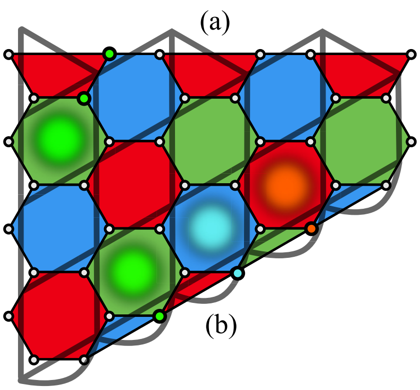

FIG. 27. Two forms of the boundaries on the 6-6-6 color code: (a) Boundaries that condense a single color, in this case green. (b) Boundaries that condense a single Pauli charge, determined by which stabilizers are removed from the boundary group. Overlayed is the rhomboidal lattice used to construct the correspondence with the cubic code boundaries. Circles on the faces indicate charges, while colored circles on the vertices indicate acting with an X (or equivalently Z) Pauli operator.

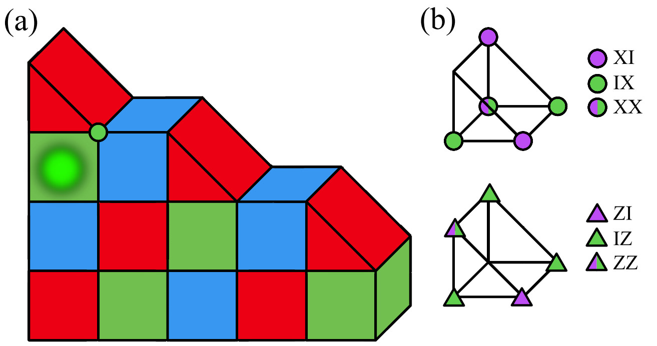

FIG. 28. (a) A boundary on the (100) face of the cubic code, which condenses only one charge type, such as m_A. The excitation and coloring shown are equivalent to that in Fig. 27. (b) The two forms of the stabilizers that are placed along the boundary. Note that the two terms anticommute when on the same location, but commute when neighboring in the x direction.

layer. In the next layer down, the residual charge is $e_A^3 \sim e_A$ and therefore nontrivial. This gives $z_{\max}(3) = 1$, and we denote this operator O_3.

For $L = 6$, we repeat O_3 twice, producing the excitation pattern in Fig. 26(b). Notably, each excitation in Fig. 26(a) is now paired with another excitation, separated by a distance $\Delta = 3$ horizontally. We thus apply O_3 onto each of the six excitation locations to the left of the dashed line, annihilating them. The residual charge created by this action produces the pattern in Fig. 26(d). As predicted by Lemma 1, this is the same as that in Fig. 26(a), but scaled by a factor of 2. We now have a nontrivial residual charge in the third layer from the top, giving $z_{\max}(6) = 2$. We denote this operator as O_6.

For $L = 9$, we cannot simply repeat O_6 twice. Instead, to annihilate all excitations in the topmost layer we must apply O_3 three times. Unlike with O_6, the residual net charge in the second layer is now nontrivial since the residual charge from O_3 is repeated thrice. We therefore again get that $z_{\max}(9) = z_{\max}(3) = 1$.

This process can be continued for arbitrary L. For each, $z_{\max}$ is determined by the largest-support operator O_j such that $j|L$, where $j = 3, 6, 12, 24, \ldots = 3 \times 2^z$ for $z \in \mathbb{Z}$. Moreover, by Lemma 1 each O_j is equivalent to $O_{j/2}$ scaled by a factor of 2, and therefore extends twice as far before reaching nontrivial residual charge. Since O_3 produces $z_{\max} = 1$, we thus get that O_j produces $z_{\max} = j/3$.

This gives the result

$$z_{\max}(L) = \max\{2^z \,:\, (3 \cdot 2^z | L),\, z \in \mathbb{Z}\} \tag{C1}$$

for $3|L$, and $z_{\max}(L) = 0$ otherwise, as required.

Although this proof relied on a square lattice, it can be generalized to an arbitrary L_x, L_y by taking the minimum of $z_{\max}(L_x)$ and $z_{\max}(L_y)$. Moreover, although we used here a diagonal G operator, equivalent fractal behavior emerges for operators confined to planes, such as the F operators used in the body of this paper.

2. Color code correspondence

As discussed in Sec. III A 1, there is a direct correspondence between the (e_{ABC}) and (m_{ABC}) boundaries, and the (2 + 1)D color code. Reference [53] showed that these color codes have six distinct gapped boundaries, defined by their Lagrangian subgroups [71]. We should therefore be able to identify equivalent representations in the boundary layers of the cubic code. Two of these boundaries directly correspond to the e and m-condensing edges of the cubic code discussed in the body of this manuscript. A third corresponds to taking products of X and Z stabilizers such that a combined *em* particle condenses. The remaining three, however, represent distinct behavior not discussed previously. In the color code, these three additional boundaries condense just red, green, or blue anyons, as in Fig. 27. Correspondingly, in the cubic code, we should observe the condensation of just A, B, or C charges. These boundaries are shown in Fig. 28. Notably, the new X and Z stabilizer terms anticommute when at the same location, but commute when placed adjacent on the x direction. Therefore, we can construct a full (3 + 1)D model with this boundary by alternating the X and Z stabilizers corresponding to the triangular prisms.

It remains an open question how these boundaries affect the encoding properties of the cubic code model. Moreover, future works should investigate the generalization of color code twist defects [53] to the cubic code model, and how their results interplay with the analysis of twists conducted in this paper.

[1] P. W. Shor, Scheme for reducing decoherence in quantum computer memory, Phys. Rev. A **52**, R2493 (1995).

[2] A. M. Steane, Error correcting codes in quantum theory, Phys. Rev. Lett. **77**, 793 (1996).

[3] P. Shor, Fault-tolerant quantum computation, in *Proceedings of 37th Conference on Foundations of Computer Science* (1996), pp. 56–65.

[4] J. Preskill, Fault-Tolerant Quantum Computation, in *Introduction to Quantum Computation and Information* (World Scientific, Singapore, 1998), pp. 213–269.

[5] A. Y. Kitaev, Fault-tolerant quantum computation by anyons, Ann. Phys. **303**, 2 (2003).

[6] S. B. Bravyi and A. Y. Kitaev, Quantum codes on a lattice with boundary, arXiv:quant-ph/9811052.

[7] E. Dennis, A. Kitaev, A. Landahl, and J. Preskill, Topological quantum memory, J. Math. Phys. **43**, 4452 (2002).

[8] B. J. Brown, D. Loss, J. K. Pachos, C. N. Self, and J. R. Wootton, Quantum memories at finite temperature, Rev. Mod. Phys. **88**, 045005 (2016).

[9] Z. Nussinov and G. Ortiz, Autocorrelations and thermal fragility of anyonic loops in topologically quantum ordered systems, Phys. Rev. B **77**, 064302 (2008).

[10] R. Alicki, M. Fannes, and M. Horodecki, On thermalization in Kitaev's 2D model, J. Phys. A: Math. Theor. **42**, 065303 (2009).

[11] S. Bravyi and B. Terhal, A no-go theorem for a two-dimensional self-correcting quantum memory based on stabilizer codes, New J. Phys. **11**, 043029 (2009).

[12] Z. Nussinov and G. Ortiz, Sufficient symmetry conditions for topological quantum order, Proc. Natl. Acad. Sci. USA **106**, 16944 (2009).

[13] Z. Nussinov and G. Ortiz, A symmetry principle for topological quantum order, Ann. Phys. **324**, 977 (2009).

[14] S. Bravyi, D. Poulin, and B. Terhal, Tradeoffs for reliable quantum information storage in 2D systems, Phys. Rev. Lett. **104**, 050503 (2010).

[15] R. Alicki, M. Horodecki, P. Horodecki, and R. Horodecki, On thermal stability of topological qubit in Kitaev's 4D model, Open Syst. Info. Dynam. **17**, 1 (2010).

[16] B. Yoshida, Feasibility of self-correcting quantum memory and thermal stability of topological order, Ann. Phys. **326**, 2566 (2011).

[17] J. Haah and J. Preskill, Logical-operator tradeoff for local quantum codes, Phys. Rev. A **86**, 032308 (2012).

[18] O. Landon-Cardinal and D. Poulin, Local topological order inhibits thermal stability in 2D, Phys. Rev. Lett. **110**, 090502 (2013).

[19] J. Haah, Local stabilizer codes in three dimensions without string logical operators, Phys. Rev. A **83**, 042330 (2011).

[20] J. Haah, Lattice quantum codes and exotic topological phases of matter, arXiv:1305.6973.

[21] C. Chamon, Quantum glassiness in strongly correlated clean systems: An Example of topological overprotection, Phys. Rev. Lett. **94**, 040402 (2005).

[22] S. Bravyi, B. Leemhuis, and B. M. Terhal, Topological order in an exactly solvable 3D spin model, Ann. Phys. **326**, 839 (2011).

[23] C. Castelnovo and C. Chamon, Topological quantum glassiness, Philos. Mag. **92**, 304 (2012).

[24] I. H. Kim, 3D local qupit quantum code without string logical operator, arXiv:1202.0052.

[25] B. Yoshida, Exotic topological order in fractal spin liquids, Phys. Rev. B **88**, 125122 (2013).

[26] S. Vijay, J. Haah, and L. Fu, A new kind of topological quantum order: A dimensional hierarchy of quasiparticles built from stationary excitations, Phys. Rev. B **92**, 235136 (2015).

[27] S. Vijay, J. Haah, and L. Fu, Fracton topological order, generalized lattice gauge theory and duality, Phys. Rev. B **94**, 235157 (2016).

[28] D. J. Williamson, Fractal symmetries: Ungauging the cubic code, Phys. Rev. B **94**, 155128 (2016).

[29] S. Bravyi and J. Haah, On the energy landscape of 3D spin Hamiltonians with topological order, Phys. Rev. Lett. **107**, 150504 (2011).

[30] H. Bombin, Topological order with a twist: Ising anyons from an Abelian model, Phys. Rev. Lett. **105**, 030403 (2010).

[31] B. J. Brown, K. Laubscher, M. S. Kesselring, and J. R. Wootton, Poking holes and cutting corners to achieve Clifford gates with the surface code, Phys. Rev. X **7**, 021029 (2017).

[32] D. Bulmash and T. Iadecola, Braiding and gapped boundaries in fracton topological phases, Phys. Rev. B **99**, 125132 (2019).

[33] Z. Weinstein, E. Cobanera, G. Ortiz, and Z. Nussinov, Absence of finite temperature phase transitions in the X-cube model and its $\mathbb{Z}_p$ generalization, Ann. Phys. **412**, 168018 (2020).

[34] H. Bombin and M. A. Martin-Delgado, Topological quantum distillation, Phys. Rev. Lett. **97**, 180501 (2006).

[35] D. Bacon, Operator quantum error correcting subsystems for self-correcting quantum memories, Phys. Rev. A **73**, 012340 (2006).

[36] D. Poulin, Stabilizer formalism for operator quantum error correction, Phys. Rev. Lett. **95**, 230504 (2005).

[37] A. R. Calderbank, E. M. Rains, P. W. Shor, and N. J. A. Sloane, Quantum error correction and orthogonal geometry, Phys. Rev. Lett. **78**, 405 (1997).

[38] D. Gottesman, The Heisenberg representation of quantum computers, *Proceedings of the XXII International Colloquium on Group Theoretical Methods in Physics*, edited by S. P. Corney, R. Delbourgo, and P. D. Jarvis (Cambridge, MA, International Press, 1999), pp. 32–43.

[39] X. G. Wen, Topological orders in rigid states, Int. J. Mod. Phys. B **04**, 239 (1990).

[40] S. Bravyi, M. B. Hastings, and S. Michalakis, Topological quantum order: Stability under local perturbations, J. Math. Phys. **51**, 093512 (2010).

[41] X.-G. Wen, Colloquium: Zoo of quantum-topological phases of matter, Rev. Mod. Phys. **89**, 041004 (2017).

[42] S. Roberts and S. D. Bartlett, Symmetry-protected self-correcting quantum memories, Phys. Rev. X **10**, 031041 (2020).

[43] H. Bombin, R. W. Chhajlany, M. Horodecki, and M. A. Martin-Delgado, Self-correcting quantum computers, New J. Phys. **15**, 055023 (2013).

[44] Z. Weinstein, G. Ortiz, and Z. Nussinov, Universality classes of stabilizer code Hamiltonians, Phys. Rev. Lett. **123**, 230503 (2019).

[45] S. Chesi, B. Röthlisberger, and D. Loss, Self-correcting quantum memory in a thermal environment, Phys. Rev. A **82**, 022305 (2010).

[46] D. Becker, T. Tanamoto, A. Hutter, F. L. Pedrocchi, and D. Loss, Dynamic generation of topologically protected self-correcting quantum memory, Phys. Rev. A **87**, 042340 (2013).

[47] C. G. Brell, A proposal for self-correcting stabilizer quantum memories in 3 dimensions (or slightly less), New J. Phys. **18**, 013050 (2016).

[48] S. Bravyi and J. Haah, Analytic and numerical demonstration of quantum self-correction in the 3D Cubic Code, Phys. Rev. Lett. **111**, 200501 (2013).

[49] J. Haah, Commuting pauli Hamiltonians as maps between free modules, Commun. Math. Phys. **324**, 351 (2013).

[50] D. E. Gottesman, Stabilizer Codes and Quantum Error Correction, Ph.D. thesis, California Institute of Technology, 1997.

[51] A. Dua, I. H. Kim, M. Cheng, and D. J. Williamson, Sorting topological stabilizer models in three dimensions, Phys. Rev. B **100**, 155137 (2019).

[52] H. Bombín, Gauge color codes: Optimal transversal gates and gauge fixing in topological stabilizer codes, New J. Phys. **17**, 083002 (2015).

[53] M. S. Kesselring, F. Pastawski, J. Eisert, and B. J. Brown, The boundaries and twist defects of the color code and their applications to topological quantum computation, Quantum **2**, 101 (2018).

[54] A. Dua, D. J. Williamson, J. Haah, and M. Cheng, Compactifying fracton stabilizer models, Phys. Rev. B **99**, 245135 (2019).

[55] H. Bombin, Topological subsystem codes, Phys. Rev. A **81**, 032301 (2010).

[56] B. J. Brown, S. D. Bartlett, A. C. Doherty, and S. D. Barrett, Topological entanglement entropy with a twist, Phys. Rev. Lett. **111**, 220402 (2013).

[57] M. Barkeshli, P. Bonderson, M. Cheng, and Z. Wang, Symmetry fractionalization, defects, and gauging of topological phases, Phys. Rev. B **100**, 115147 (2019).

[58] Y. You, Non-Abelian defects in fracton phases of matter, Phys. Rev. B **100**, 075148 (2019).

[59] M. Barkeshli, Y.-A. Chen, S.-J. Huang, R. Kobayashi, N. Tantivasadakarn, and G. Zhu, Codimension 2 defects and higher symmetries in (3+1)D topological phases, SciPost Phys. **14**, 065 (2023).

[60] A. Krishna and D. Poulin, Topological wormholes: Nonlocal defects on the toric code, Phys. Rev. Res. **2**, 023116 (2020).

[61] N. Manoj, K. Slagle, W. Shirley, and X. Chen, Screw dislocations in the X-cube fracton model, SciPost Phys. **10**, 094 (2021).

[62] J. Haah, L. Fidkowski, and M. B. Hastings, Nontrivial quantum cellular automata in higher dimensions, Commun. Math. Phys. **398**, 469 (2023).

[63] W. Ji and X. G. Wen, Noninvertible anomalies and mapping-class-group transformation of anomalous partition functions, Phys. Rev. Res. **1**, 033054 (2019).

[64] B. Yoshida, Gapped boundaries, group cohomology and fault-tolerant logical gates, Ann. Phys. **377**, 387 (2017).

[65] T. Devakul, Classifying local fractal subsystem symmetry-protected topological phases, Phys. Rev. B **99**, 235131 (2019).

[66] D. J. Williamson and T. Devakul, Type-II fractons from coupled spin chains and layers, Phys. Rev. B **103**, 155140 (2021).

[67] T. Devakul and D. J. Williamson, Fractalizing quantum codes, Quantum **5**, 438 (2021).

[68] K. Slagle, D. Aasen, and D. Williamson, Foliated field theory and string-membrane-net condensation picture of fracton order, SciPost Phys. **6**, 043 (2019).

[69] D. Aasen, D. Bulmash, A. Prem, K. Slagle, and D. J. Williamson, Topological defect networks for fractons of all types, Phys. Rev. Res. **2**, 043165 (2020).

[70] Z. Song, A. Dua, W. Shirley, and D. J. Williamson, Topological defect network representations of fracton stabilizer codes, PRX Quant. **4**, 010304 (2023).

[71] M. Levin, Protected edge modes without symmetry, Phys. Rev. X **3**, 021009 (2013).

[72] S. Beigi, P. W. Shor, and D. Whalen, The quantum double model with boundary: Condensations and symmetries, Commun. Math. Phys. **306**, 663 (2011).

[73] A. Kitaev and L. Kong, Models for gapped boundaries and domain walls, Commun. Math. Phys. **313**, 351 (2012).

[74] L. Kong, Anyon condensation and tensor categories, Nucl. Phys. B **886**, 436 (2014).

[75] S. Pai and M. Hermele, Fracton fusion and statistics, Phys. Rev. B **100**, 195136 (2019).

[76] H. Song, N. Tantivasadakarn, W. Shirley, and M. Hermele, Fracton self-statistics, Phys. Rev. Lett. **132**, 016604 (2024).

[77] S. Vijay and L. Fu, A generalization of non-Abelian anyons in three dimensions, arXiv:1706.07070.

[78] A. Prem, S. J. Huang, H. Song, and M. Hermele, Cage-net fracton models, Phys. Rev. X **9**, 021010 (2019).

[79] H. Song, A. Prem, S. J. Huang, and M. A. Martin-Delgado, Twisted fracton models in three dimensions, Phys. Rev. B **99**, 155118 (2019).

[80] A. Prem and D. Williamson, Gauging permutation symmetries as a route to non-Abelian fractons, SciPost Phys. **7**, 068 (2019).

[81] D. Bulmash and M. Barkeshli, Gauging fractons: Immobile non-Abelian quasiparticles, fractals, and position-dependent degeneracies, Phys. Rev. B **100**, 155146 (2019).

[82] D. J. Williamson and M. Cheng, Designer non-Abelian fractons from topological layers, Phys. Rev. B **107**, 035103 (2023).

[83] J. Sullivan, T. Iadecola, and D. J. Williamson, Planar p-string condensation: Chiral fracton phases from fractional quantum Hall layers and beyond, Phys. Rev. B **103**, 205301 (2021).

[84] N. Tantivasadakarn, W. Ji, and S. Vijay, Non-Abelian hybrid fracton orders, Phys. Rev. B **104**, 115117 (2021).

[85] B. J. Brown and D. J. Williamson, Parallelized quantum error correction with fracton topological codes, Phys. Rev. Res. **2**, 013303 (2020).

[86] D. V. Else and R. Thorngren, Crystalline topological phases as defect networks, Phys. Rev. B **99**, 115116 (2019).

[87] G. Evenbly and G. Vidal, Class of highly entangled many-body states that can be efficiently simulated, Phys. Rev. Lett. **112**, 240502 (2014).

[88] J. Haah, Bifurcation in entanglement renormalization group flow of a gapped spin model, Phys. Rev. B **89**, 075119 (2014).

[89] W. Shirley, K. Slagle, Z. Wang, and X. Chen, Fracton models on general three-dimensional manifolds, Phys. Rev. X **8**, 031051 (2018).

[90] A. Dua, P. Sarkar, D. J. Williamson, and M. Cheng, Bifurcating entanglement-renormalization group flows of fracton stabilizer models, Phys. Rev. Res. **2**, 033021 (2019).

[91] https://github.com/corytaitchison/cubic-code

[92] A. Yu. Kitaev, Quantum Error Correction with Imperfect Gates, in *Quantum Communication, Computing, and Measurement*, edited by O. Hirota, A. S. Holevo, and C. M. Caves (Springer US, Boston, MA, 1997), pp. 181–188.

[93] H. Alloul, J. Bobroff, M. Gabay, and P. J. Hirschfeld, Defects in correlated metals and superconductors, Rev. Mod. Phys. **81**, 45 (2009).